Developmental Cell
Article

Autophagosome Biogenesis in Primary Neurons Follows an Ordered and Spatially Regulated Pathway

Sandra Maday[1] and Erika L.F. Holzbaur[1,*]
[1]Department of Physiology, Perelman School of Medicine, University of Pennsylvania, Philadelphia, PA 19104, USA
*Correspondence: holzbaur@mail.med.upenn.edu
http://dx.doi.org/10.1016/j.devcel.2014.06.001

SUMMARY

Autophagy is an essential degradative pathway in neurons, yet little is known about mechanisms driving autophagy in highly polarized cells. Here, we use dual-color live-cell imaging to investigate the neuron-specific mechanisms of constitutive autophagosome biogenesis in primary dorsal root ganglion (DRG) and hippocampal cultures. Under basal conditions, autophagosomes are continuously generated in the axon tip. There is an ordered assembly of proteins recruited with stereotypical kinetics onto the developing autophagosome. Plasma- or mitochondrial-derived membranes were not incorporated into nascent autophagosomes in the distal axon. Rather, autophagosomes are generated at double FYVE-containing protein 1 (DFCP1)-positive subdomains of the endoplasmic reticulum (ER), distinct from ER exit sites. Biogenesis events are enriched distally; autophagosomes form infrequently in dendrites, the soma, or midaxon, consistent with a compartmentalized pathway for constitutive autophagy in primary neurons. Distal biogenesis may facilitate degradation of damaged mitochondria and long-lived cytoplasmic proteins reaching the axon tip via slow axonal transport.

INTRODUCTION

Macroautophagy (autophagy) is an evolutionarily conserved lysosomal degradation pathway that maintains the homeostasis of the cellular environment by eliminating damaged organelles and aggregated proteins (Xie and Klionsky, 2007). This pathway is particularly important in postmitotic cells such as neurons that are unable to dilute out proteotoxins by cell division. CNS-specific or neuron-specific knockout of genes required for autophagy induces axonal degeneration and neuron cell death (Hara et al., 2006; Komatsu et al., 2006, 2007). Furthermore, mutations in the mitophagy machinery PINK1 and Parkin lead to early-onset Parkinson's disease (Kitada et al., 1998; Narendra et al., 2008, 2010; Valente et al., 2004), potentially linking defective autophagy with the progression of neurodegenerative disease. Autophagy is thus a protective mechanism against neuronal dysfunction and degeneration (Mariño et al., 2011; Rubinsztein et al., 2005).

Despite the evidence that autophagy is critical in maintaining neuronal homeostasis, little is understood about the mechanisms driving this process in neurons. Much of the work dissecting the autophagic pathway has been performed in yeast and nonpolarized mammalian cells (Mizushima et al., 2011; Weidberg et al., 2011). However, neurons exhibit a highly polarized and elongated morphology that poses a unique challenge to cellular trafficking and transport pathways. Many neurodegenerative disease-associated mutations have been identified in the machinery that transports organelles and proteins across the extended distance of the axon (Millecamps and Julien, 2013; Perlson et al., 2010), emphasizing the unique vulnerability of the neuronal system. Furthermore, the majority of studies to date have focused on stress-induced autophagy as a result of nutrient deprivation. However, knockout mouse models have demonstrated that basal levels of autophagy are essential for neuronal survival (Hara et al., 2006; Komatsu et al., 2006, 2007). Thus, we set out to determine the spatiotemporal dynamics of autophagy in primary neurons under basal growth conditions.

Here, we describe the assembly of an autophagosome in real time in primary dorsal root ganglion (DRG) and hippocampal neurons. We find that autophagosome formation in primary neurons is a constitutive process under basal growth conditions. Autophagosomes are continuously generated at the axon tip; this biogenesis involves an ordered recruitment of proteins that assemble onto the nascent autophagosome with stereotypical kinetics. Under basal conditions, we find that neuronal autophagosomes are not generated from plasma- or mitochondrial-derived membrane but, rather, from specific subdomains of the endoplasmic reticulum (ER). Most strikingly, autophagosomes are preferentially generated at the distal end of the axon, emphasizing the high degree of compartmentalization and spatial regulation controlling autophagosome biogenesis in primary neurons. We propose that this pathway provides a mechanism to recycle distally localized aged mitochondria as well as long-lived proteins transported to the distal axon via slow axonal transport.

RESULTS

Autophagosome Biogenesis in Primary Neurons Follows an Ordered and Spatially Regulated Pathway

Autophagy is initiated when components of the cytosol are enveloped within a membrane cisterna termed an "isolation membrane" or "phagophore" (Xie and Klionsky, 2007). The

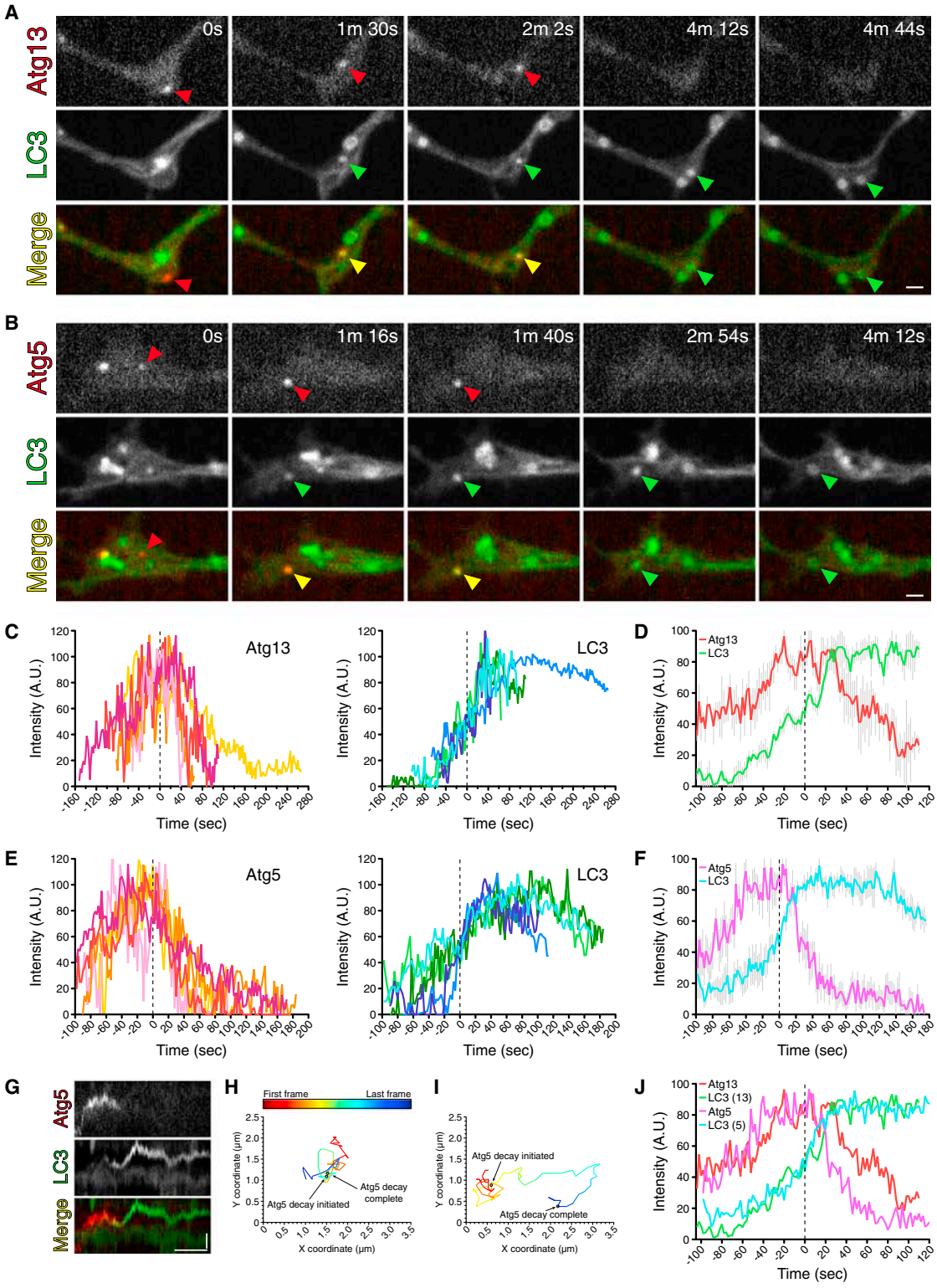

Figure 1. Autophagosome Biogenesis in DRG Neurons Involves an Ordered Recruitment of Assembly Factors

(A) Time series of mCherry-Atg13 and GFP-LC3 in the distal axon of DRG neurons. Red and green arrowheads indicate the ordered appearance of Atg13 followed by LC3, respectively. Yellow arrowheads denote colocalization between Atg13 and LC3. The retrograde direction is toward the right. Scale bar, 1 μm.

(B) Time series of mCherry-Atg5 and GFP-LC3 in the distal axon. Red and green arrowheads indicate the ordered appearance of Atg5 followed by LC3, respectively. Yellow arrowheads denote colocalization between Atg5 and LC3. The retrograde direction is toward the right. Scale bar, 1 μm. See also Movie S1.

(legend continued on next page)

edges of the isolation membrane fuse to form a closed double-membrane autophagosome. These autophagosomes are shuttled toward lysosomes for fusion, and the contents are degraded by lysosomal hydrolases and recycled back into the cytosol. Seminal work in yeast identified proteins important for the formation of an autophagosome (Harding et al., 1995; Klionsky et al., 2003; Thumm et al., 1994; Tsukada and Ohsumi, 1993), and many are conserved in mammals (Mizushima et al., 2011; Weidberg et al., 2011). During autophagosome formation, these proteins are recruited to the assembly site in an ordered fashion (Itakura and Mizushima, 2010; Suzuki et al., 2001, 2007). We set out to determine whether neurons employ this conserved mechanism for autophagosome formation and define the temporal relationship between assembly proteins as they arrive at the nascent autophagosome.

We performed live-cell imaging on DRG neurons isolated from transgenic mice expressing GFP-LC3. To measure autophagosome assembly, neurons were transfected with either Atg13 or Atg5 labeled with mCherry to allow pairwise imaging with GFP-LC3. Atg13 is a component of the Ulk1 complex that regulates initial formation of the autophagosome (Mizushima et al., 2011) and Atg5 localizes to the isolation membrane and regulates its elongation (Mizushima et al., 2001). Thus, both Atg13 and Atg5 identify the initial stages of autophagosome formation. In all experiments, only those neurons with low Atg13 or Atg5 expression were imaged in order to observe specific events of biogenesis.

In primary DRG neurons, we observed the appearance of puncta positive for Atg13 that grew progressively in size (Figure 1A). These structures appeared almost exclusively in the distal end of the axon. Following Atg13 arrival, LC3 was recruited to nascent autophagosomes. Atg13 then dissociated, leaving LC3-positive puncta to grow progressively into ring structures ~800 nm in diameter. We observed the same pattern of ordered recruitment between Atg5 and LC3 (Figure 1B; Movie S1 available online). Atg5 appeared initially, followed by LC3. After a period of overlap, the Atg5 signal decayed from nascent autophagosomes, whereas the LC3 puncta grew into ring structures (Figure 1B; Movie S1). Occasionally, we observed LC3-positive cup-shaped structures representing the isolation membrane (Figure S1). Kymograph analysis of single biogenesis events clearly reveals the sequential appearance of Atg5 followed by LC3 in the distal axon (Figure 1G). Together, these results indicate that neuronal autophagosomes are generated by an ordered recruitment of assembly factors.

To resolve the temporal relationship between the recruitment of assembly factors, we quantitated the fluorescence intensity of Atg13 or Atg5 relative to that of LC3 over time. As shown in Figures 1C–1F, the hierarchical recruitment of assembly factors proceeds with highly consistent kinetics. On average, Atg13 and Atg5 reached a maximum intensity within ~1.3 and ~1.0 min after initial appearance, respectively, and sustained that signal for ~50 s before decay was initiated (Figures 1C–1F). Alignment of Atg13 and Atg5 mean intensity profiles indicated that they are recruited to nascent autophagosomes with kinetics that cannot be distinguished at this time resolution (one frame every 2 s; Figure 1J). However, Atg5 decayed from the nascent autophagosome prior to Atg13 (Figure 1J). This order of disassembly from the nascent autophagosome was also observed with direct pairwise imaging of GFP-Atg13 and mCherry-Atg5 (data not shown). The dynamics of LC3 intensity changes over time measured across all experiments were extraordinarily consistent. Following a lag phase, LC3 was robustly recruited, rising from initial signal to maximum intensity within 1.5 min (Figures 1C–1F and 1J). Decay of Atg5 was always initiated prior to observation of maximum LC3 intensity at the developing autophagosome (Figures 1F and 1J).

Next, we asked whether there is a relationship between the stage of autophagosome formation and the mobility of the structure. We hypothesized that perhaps during the Atg5-positive phase, the autophagosome is confined due to tethering to the membrane source. Upon release of the closed autophagosome (Atg5-negative phase), the compartment may become more motile. To examine this possibility, we plotted the tracks exhibited by each biogenesis event. For two out of four biogenesis events, developing autophagosomes moved within a confined region within the distal process (representative example in Figure 1H). For the remaining two events, developing autophagosomes exhibited two phases of motility. Initially during the Atg5-positive phase, the nascent autophagosome exhibited a period of confined motility that was followed by a period of more unrestricted motility during the LC3-dominant phase (representative example in Figure 1I). This transition in motility may coincide with fusion of the isolation membrane and release of the closed autophagosome. This sequence of events was only clearly observed in a subset of biogenesis events tracked, but our resolution may be limited due to imaging in only a single focal plane.

Our previous observations on GFP-LC3 dynamics in primary neurons suggested that autophagosomes preferentially initiate distally (Maday et al., 2012). To examine this question more rigorously, we measured the localization of autophagosome biogenesis within the neuron, determining the number of autophagosomes that form in the distal axon, midaxon, and cell soma by monitoring either Atg13 or Atg5 (Figure 2A). Strikingly, constitutive autophagosomes were generated almost exclusively in the distal end of the axon (Figures 2B–2E). Comparing

(C) Intensity profiles of mCherry-Atg13 and GFP-LC3 from five individual biogenesis events. Vertical dashed line denotes the half-maximum in LC3 intensity, which was used to align the traces.
(D) Mean intensity profile of mCherry-Atg13 and GFP-LC3 (mean ± SEM; n = 5 biogenesis events from five neurons from three separate experiments).
(E) Intensity profiles of mCherry-Atg5 and GFP-LC3 from five individual biogenesis events.
(F) Mean intensity profile of mCherry-Atg5 and GFP-LC3 (mean ± SEM; n = 5 biogenesis events from three neurons from three separate experiments).
(G) Kymograph showing the ordered recruitment of mCherry-Atg5 followed by GFP-LC3 to nascent autophagosomes in the distal axon. Horizontal bar, 1 min. Vertical bar, 1 μm.
(H and I) Trajectories of two autophagosome biogenesis events. Tracks are color coded for time: first frame is red; last frame is blue.
(J) Alignment of Atg13 and LC3 mean intensity profiles with Atg5 and LC3 mean intensity profiles. Vertical dashed line marks the LC3 half-maximum to which the traces were aligned.

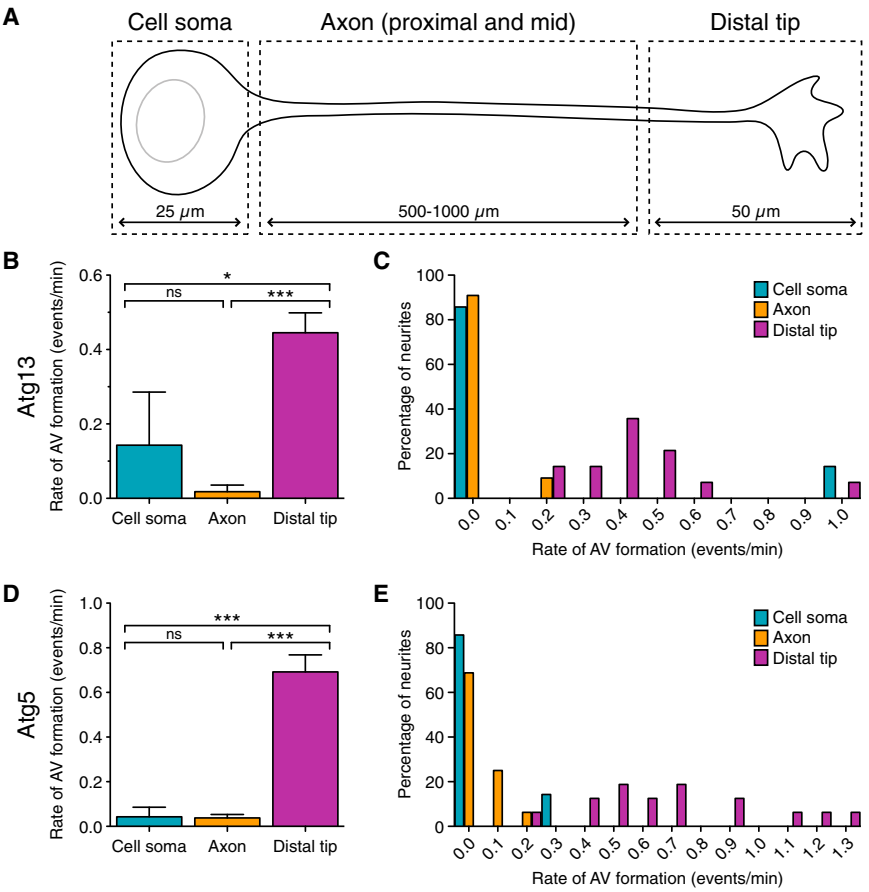

Figure 2. Autophagosome Biogenesis in Primary Neurons Is Enriched in the Distal Axon of DRG Neurons

(A) Schematic of a DRG neuron. The boxed regions designate the cell soma, axon, and distal tip where rates of autophagosome formation were measured. The distal tip encompassed the terminal ~50 μm of the axon. Autophagosome formation along the axon (500–1,000 μm in length) was quantified within an ~80 μm observation window. The cell soma encompassed a diameter of ~25 μm. Despite the difference in length, biogenesis rates in the axon and distal tip were measured within equivalent cross-sectional areas.

(B) Mean rates of autophagosome formation (measured with mCherry-Atg13 and GFP-LC3) in the cell soma, axon, and distal tip (mean ± SEM; cell soma, n = 7 neurons from 3 experiments; axon, n = 11 axons from 8 neurons and 4 experiments; distal tip, n = 14 tips from 12 neurons and 4 experiments), ns, not significant. *p < 0.05; ***p < 0.001 (one-way ANOVA with Tukey's post hoc test).

(C) Distribution of individual biogenesis rates in each domain as measured with mCherry-Atg13.

(D) Mean rates of autophagosome formation (measured with mCherry-Atg5 and GFP-LC3) in the cell soma, axon, and distal tip (mean ± SEM; cell soma, n = 7 neurons from 2 experiments; axon, n = 16 axons from 13 neurons and 3 experiments; distal tip, n = 16 tips from 16 neurons and 5 experiments). ns, not significant. ***p < 0.001 (one-way ANOVA with Tukey's post hoc test).

(E) Distribution of individual biogenesis rates in each domain as measured with mCherry-Atg5.

equivalent cross-sectional areas, the mean rate of autophagosome formation in the distal axon was ~20-fold higher than observed along the midaxon (Figures 2B and 2D). In the distal axon, autophagosome biogenesis was observed in all neurons with rates ranging from 0.2 to 1.3 autophagosomes formed per min (Figures 2C and 2E). In contrast, ~70%–90% of neurons displayed no biogenesis along the midaxon during our observation period, with the remaining neurons exhibiting biogenesis rates ≤0.2 autophagosomes per min (Figures 2C and 2E). In the cell body, rates of formation were more variable, potentially due to imaging in a single focal plane within the ~5 μm depth of the soma. Of neurons, 86% displayed no biogenesis events in the cell body (Figures 2B–2E). LC3-positive autophagosomes are clearly present along the midaxon and in the cell soma, but we did not observe robust formation in either of these regions under basal conditions. Thus, constitutive autophagy occurs preferentially at the distal end of the axon in primary DRG neurons.

Autophagosomes Also Form Distally and Undergo Retrograde Transport in Axons of Synaptically Connected Neurons

DRG neurons are a well-established model system for neurite development. However, these cells actively extend processes and do not form synapses as a monoculture in vitro. Thus, we investigated whether the dynamics observed in DRG neurons are also seen in a culture that becomes synaptically connected. To explore this possibility, we measured autophagosome biogenesis and transport along the axons of hippocampal neurons cultured up to 16 days in vitro (DIV).

At 7 DIV, hippocampal neurons exhibit well-defined axon and dendrite projections (Figure 3A), as defined morphologically and confirmed by microtubule-associated protein 2 and tau immunostaining (data not shown). By 10 DIV, excitatory synapses are evident (Figure S2). Autophagosomes were detected along the length of the axon and in the cell soma of hippocampal neurons (Figure 3A). Live-cell imaging of the distal axon revealed active autophagosome formation with the appearance of GFP-LC3-positive puncta that grew into ring structures (Figure 3B). Quantitation of the rates of biogenesis showed an enrichment of autophagosome formation in the distal axon as compared with the midaxon (Figure 3B). Biogenesis rates in either the mid or distal axon did not change with age of the culture; similar rates were observed at either young (5 DIV) or synaptically connected (10 DIV) stages of development (Figure 3B). In fact, robust distal biogenesis continued to be observed in neurons 2 weeks in vitro (data not shown). Autophagosome formation in the cell soma was occasionally observed, but measurement of biogenesis rates in this region of the cell was limited by the depth of the soma.

Similar to our previous observations in DRG neurons (Maday et al., 2012), autophagosomes that formed in the distal axon of hippocampal neurons initially move bidirectionally, then switch to robust processive, primarily unidirectional movement along

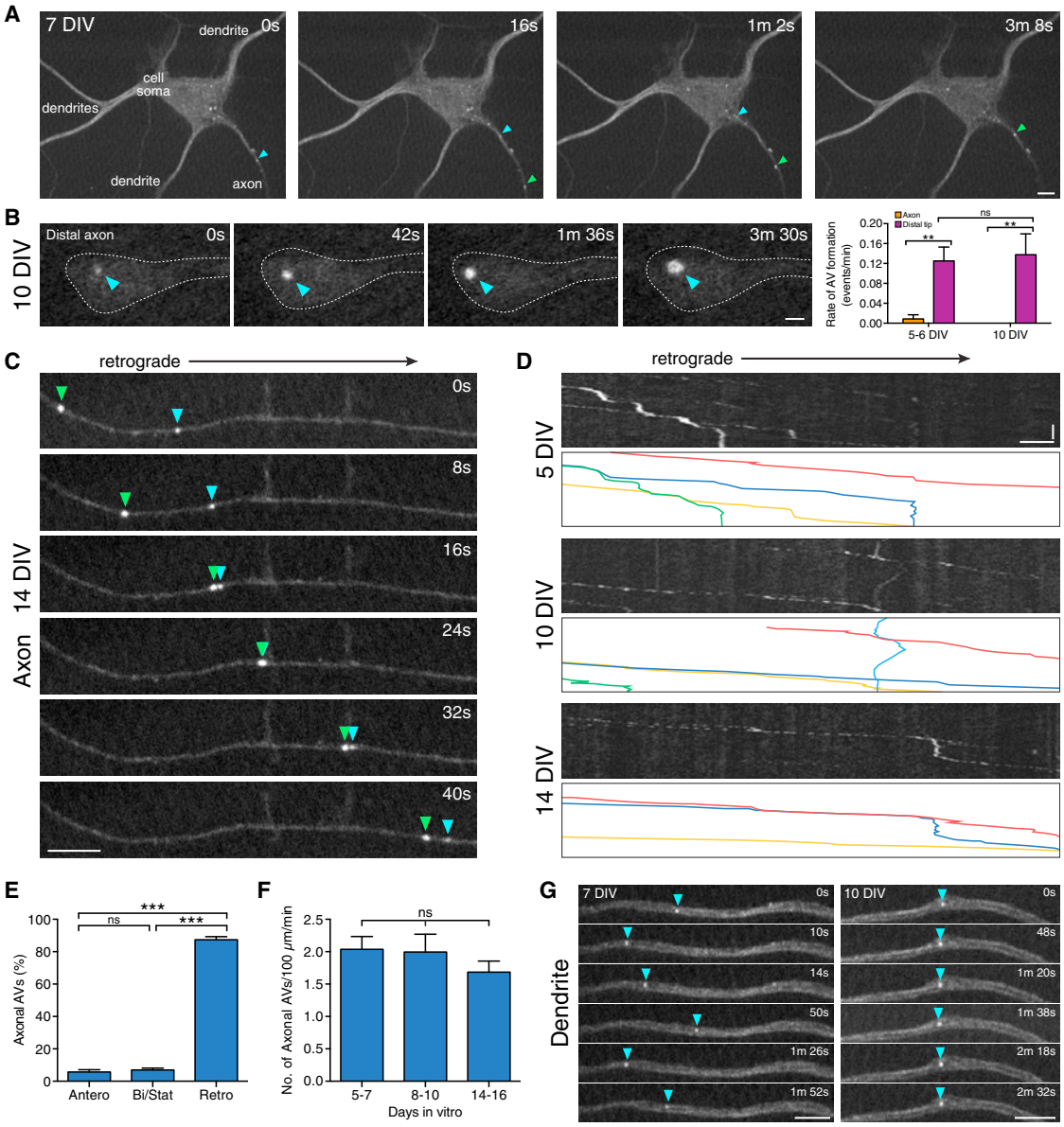

Figure 3. Autophagosomes Form in the Distal Axon and Undergo Retrograde Transport toward the Cell Soma in Hippocampal Neurons

(A) Hippocampal neurons grown 7 DIV form axon and dendrite processes. Arrowheads denote autophagosomes undergoing retrograde transport in the axon and entering the cell soma. Scale bar, 5 μm.

(B) Time series of autophagosome biogenesis in the distal axon of hippocampal neurons grown 10 DIV. Arrowheads denote appearance of a GFP-LC3-positive punctum that grows into a ring structure. Scale bar, 1 μm. Also shown is the mean rate of autophagosome biogenesis in the mid versus distal axon (mean ± SEM; 5–6 DIV, n = 12 neurons from 3 experiments; 10 DIV, n = 8–9 neurons from 2 experiments). ns, not significant. **p < 0.01 (two-way ANOVA with Tukey's post hoc test).

(C) Time series of retrograde autophagosome motility in the axon of hippocampal neurons at 14 DIV. Arrowheads denote two retrograde autophagosomes. Scale bar, 5 μm.

(D) Kymographs of autophagosome motility at various developmental stages. For clarity, the kymographs were traced and shown below each corresponding kymograph. Each autophagosome track is denoted by a different color. Horizontal bar, 5 μm. Vertical bar, 1 min.

(E) Quantitation of autophagosome motility in the axon of hippocampal neurons (5–16 DIV; mean ± SEM; n = 66 neurons from 4 experiments). ns, not significant. ***p < 0.001 (one-way ANOVA with Tukey's post hoc test).

(F) Quantitation of autophagosome flux over various developmental stages (mean ± SEM; 5–7 DIV, n = 31 neurons from 3 experiments; 8–10 DIV, n = 23 neurons from 3 experiments; 14–16 DIV, n = 12 neurons from 3 experiments). ns, not significant (one-way ANOVA with Tukey's post hoc test).

(G) Time series of bidirectional (left) and stationary (right) autophagosomes (arrowheads) in dendrites. The retrograde direction is toward the right. Scale bars, 5 μm.

the mid and proximal axon (Figure 3C). The robust retrograde transport of autophagosomes along the axon was exhibited throughout development (5–16 DIV), with 87% ± 1.9% (±SEM) of axonal autophagosomes moving a net distance of ≥5 μm in the retrograde direction (Figures 3D and 3E). Only ~6% of axonal autophagosomes moved in the anterograde direction, and ~7% exhibited nonprocessive bidirectional motility or remained stationary. Strikingly, autophagosome flux along the axon did not change with age of the culture (Figure 3F).

We find that autophagosome dynamics in the axons of hippocampal and DRG neurons are remarkably similar. The mean autophagosome flux along the axon of hippocampal neurons (5–16 DIV) was similar to our previously reported value in DRG neurons grown 2 DIV (Maday et al., 2012): 1.96 ± 0.14 (±SEM) versus 1.76 ± 0.09 (±SEM) autophagosomes within 100 μm/min, respectively. Autophagosome motility is robustly retrograde in both neuronal subtypes, with 87% ± 1.9% (±SEM) in hippocampal neurons as compared to 82% ± 2.1% (±SEM) in DRG neurons; speeds are also very similar, with 0.62 ± 0.04 (±SEM) and 0.55 ± 0.06 (±SEM) μm/s measured in hippocampal and DRG neurons, respectively. Importantly, constitutive biogenesis of autophagosomes is enriched in the distal axons of both hippocampal and DRG neurons. Thus, the overall paradigm of distal initiation followed by robust retrograde transport along the axon is similar between DRG and hippocampal neurons. The rates of biogenesis in the distal axon of hippocampal neurons, however, are ~4-fold lower as compared to DRG neurons. Because flux along the midaxon is similar between these two neuronal types, autophagosome biogenesis may be less tightly restricted to the distal axon in synaptically connected neurons as compared to developing axons undergoing robust growth. There may be more formation along the midaxon of hippocampal neurons than is detected in our assay due to low formation rates distributed over the cumulative distance of the axon. Consistent with this, we observed lower autophagosome densities in the distal region of hippocampal neurons as compared to previous observations in DRG neurons (Maday et al., 2012).

We also observed autophagosomes in the dendrites of hippocampal neurons. In contrast to the processive retrograde motility in axons, autophagosomes in dendrites exhibited predominantly nonprocessive bidirectional and stationary transport (Figure 3G). Of the 60 autophagosomes that could be unambiguously tracked within dendrites from 29 neurons, 62% were stationary, 17% exhibited bidirectional motility, 15% moved processively in the anterograde direction, and only 7% moved processively in the retrograde direction. Thus, the motility of autophagosomes within dendrites is strikingly different from what we observed along the axon and may be due to the mixed microtubule polarity within dendrites (Baas et al., 1988).

The ER Is the Major Membrane Source for Neuronal Autophagosomes

Multiple organelles have been implicated as the source of membrane for autophagosomes, including plasma membrane (Hollenbeck, 1993; Ravikumar et al., 2010), the Golgi (van der Vaart and Reggiori, 2010), mitochondria (Hailey et al., 2010), and ER (Hamasaki et al., 2013; Hayashi-Nishino et al., 2009; Ylä-Anttila et al., 2009). For neurons, generating an autophagosome in the distal axon poses a unique challenge due to the confined nature of this space that is largely devoid of the Golgi. We performed dual-color imaging of Atg13 along with various membrane markers to determine the origin of the autophagosome membrane in primary DRG neurons. We utilized two markers, the src kinase Lyn and CellMask Orange, to label the plasma membrane as well as plasma membrane-derived internal compartments (Figures 4A and 4B). Atg13 puncta appearing in the distal axon were negative for both plasma membrane markers (Figures 4A and 4B). Thus, plasma membrane-derived material is not a likely source for neuronal autophagosome membrane in the distal axon under basal conditions.

To address the possibility that mitochondria may supply membrane to nascent autophagosomes, we performed dual-color imaging with GFP-Atg13 and dsRed2-mito. We did not observe significant colocalization between Atg13 and mitochondria (Figure 4C). Although there was occasional transient overlap, there was no stable association between these compartments as assessed by kymographs (Figure 5B). Thus, mitochondria are not a primary source of membrane for neuronal autophagosomes under basal conditions.

In contrast, we did observe colocalization between Atg13 and the ER translocon subunit Sec61β. In the distal axon, Atg13 puncta appeared on or near ER structures labeled with Sec61β (Figure 5A; Movie S2). Line scans across the distal tip consistently showed peaks of Atg13 coincident with some but not all peaks of Sec61β, suggesting that specific subdomains of the ER are primed for autophagosome formation (Figure 5A). Furthermore, Atg13 and Sec61β often comigrated in the distal axon (Figure 5A), providing compelling evidence that these structures colocalize and are dynamically connected. Interestingly, as the Atg13 punctum changed shape, the underlying ER also changed shape to match that of the Atg13 punctum. To further demonstrate coordinated motility between Atg13 and the ER, we generated kymographs from each biogenesis event. Although there was no significant overlap between Atg13 and the plasma membrane or mitochondria, Atg13 and Sec61β colocalized and moved together in a coordinated fashion (Figure 5B). Together, our results demonstrate an association between the ER and developing autophagosomes.

To quantitate the degree of colocalization between Atg13 and the ER, we measured the Pearson's correlation coefficient between corresponding kymographs of Atg13 and Sec61β. The mean Pearson's coefficient value between Atg13 and the plasma membrane or mitochondria was negative and nearly zero, respectively (Figure 5C). However, the mean value measured between Atg13 and Sec61β was significantly positive, indicating colocalization between developing autophagosomes and the ER (Figure 5C). As a control, we inverted the ER kymograph horizontally and observed a significant decrease in the mean Pearson's coefficient value (Figure S3). Thus, colocalization between Atg13 and Sec61β is not simply due to the fact that the ER is widely distributed within the distal axon tip; rather, there is a specific association between these two compartments. Together, these data support a key role for the ER in providing membrane to developing autophagosomes in primary neurons under basal conditions.

Although the majority of biogenesis events originate from the ER, we noticed a minor population of events that undergo nonconventional forms of biogenesis, appearing to arise from preexisting autophagosome rings. We occasionally observed

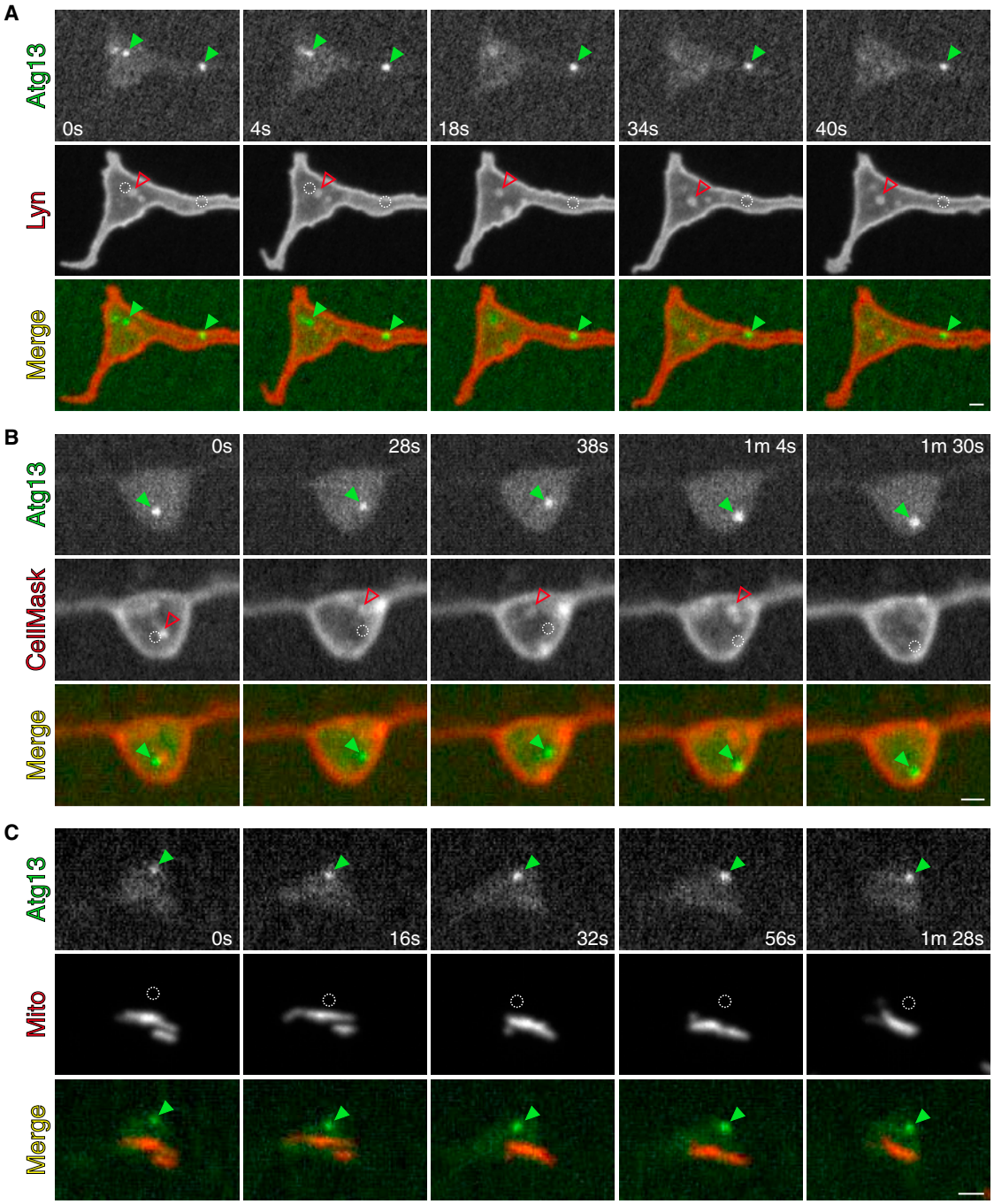

Figure 4. Plasma and Mitochondrial Membrane Are Not Incorporated into Nascent Autophagosomes

(A) Time series of mCherry-Atg13 and plasma membrane marker Lyn-GFP in the distal axon of a DRG neuron. Atg13 is pseudocolored green for consistency throughout the figure. The retrograde direction is toward the right.

(B) Time series of GFP-Atg13 and plasma membrane dye CellMask Orange. The retrograde direction is toward the right.

(C) Time series of GFP-Atg13 and mitochondrial marker dsRed2-mito. The retrograde direction is toward the left.

Throughout the figure, green arrowheads mark autophagosome biogenesis events. Dashed circles designate the location of the biogenesis event to demonstrate the absence of plasma membrane and mitochondrial markers. Despite the absence on Atg13-positive puncta, plasma membrane markers are capable of labeling internal organelles (open red arrowheads). Scale bars, 1 μm.

"buds" appearing from preexisting rings that remain attached to the parental ring, moving together in the distal axon (Figure S4). We also noticed the presence of Atg5 puncta associated with LC3 ring structures (Figure S4). These results suggest that autophagosome rings may sometimes nucleate other smaller autophagic structures.

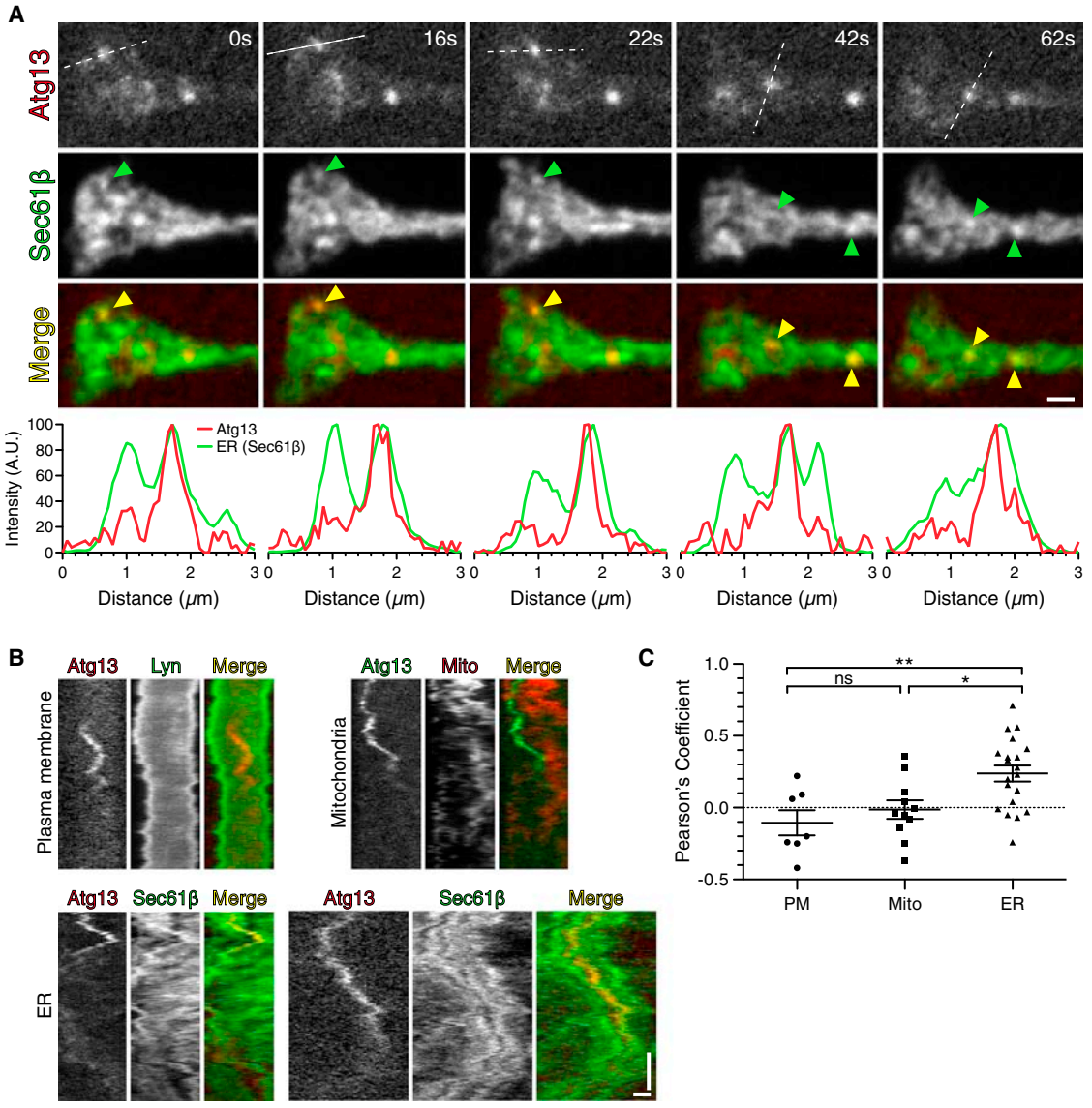

Figure 5. Neuronal Autophagosomes Form on or near the ER in the Distal Axon

(A) Time series of mCherry-Atg13 and ER marker GFP-Sec61β in the distal axon of a DRG neuron. Yellow arrowheads denote autophagosome biogenesis events that colocalize and comigrate with the ER. Green arrowheads denote regions of ER that colocalize with Atg13. The retrograde direction is toward the right. Line scans drawn across the distal axon (position marked with dashed lines) follow a single biogenesis event and indicate overlapping peaks of intensity between Atg13 and the ER. Scale bar, 1 μm. See also Movie S2.

(B) Corresponding kymographs between Atg13 and plasma membrane, mitochondria, or ER. Atg13 comigrates with the ER, suggesting that these compartments are associated. Because not all biogenesis events were captured at the start of Atg13 signal, the duration of the biogenesis event may vary. Horizontal bar, 1 μm. Vertical bar, 1 min.

(C) Scatterplot of the Pearson's correlation coefficient measured from corresponding kymographs of Atg13 and plasma membrane, mitochondria, or ER (mean ± SEM; plasma membrane, n = 7 biogenesis events from 4 neurons from a representative experiment; mitochondria, n = 11 biogenesis events from 7 neurons from a representative experiment; ER, n = 20 biogenesis events from 11 neurons from 3 experiments). ns, not significant. *$p < 0.05$; **$p < 0.01$ (one-way ANOVA with Tukey's post hoc test). Each point on the scatterplot represents one biogenesis event. Note that the sequential capture of images used here limits the maximum value of the Pearson's correlation coefficient, even for colocalized signals.

Neuronal Autophagosomes Form at DFCP1-Positive Subdomains of the ER

We next aimed to determine which subdomain of the ER plays a role in autophagosome formation. First, we explored the possibility that ER exit sites (ERESs), regions rich in coat protein complex II (COPII)-mediated membrane-budding events, contributed membrane to nascent autophagosomes. Upon expression of GFP-Sec16L, a COPII coat assembly protein (Bhattacharyya and Glick, 2007), we noticed a striking gradient of ERESs along the axon of DRG neurons. Sec16L puncta were concentrated in the cell soma and proximal axon and decreased in density in the midaxon and distal tip (Figure 6A).

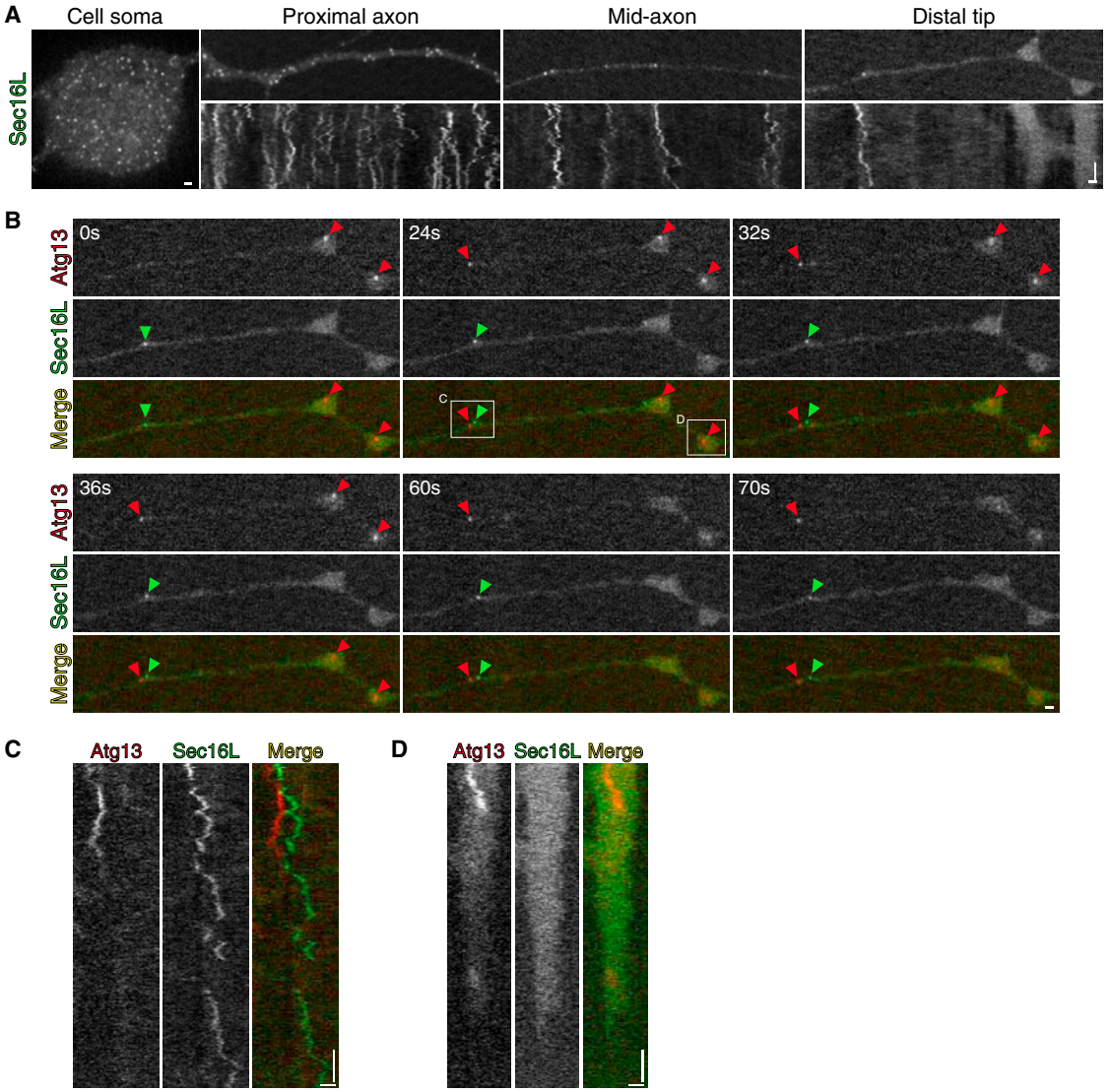

Figure 6. Neuronal Autophagosomes Do Not Form at ERESs

(A) Still images and corresponding kymographs of GFP-Sec16L in primary DRG neurons show a decreasing gradient of ERESs from the cell soma to the distal tip of the axon. ERESs are enriched in the cell soma and proximal axon and depleted from the distal axon. Kymographs show bidirectional/stationary motility of ERESs along the axon and clearly display the decreasing density of ERESs from cell soma to tip. Horizontal bars, 1 μm. Vertical bar, 1 min.

(B) Time series of mCherry-Atg13 and GFP-Sec16L in the distal axon. Red arrowheads denote biogenesis events that form at sites distinct from or absent of ERESs (green arrowheads). Scale bar, 1 μm.

(C and D) Kymographs generated from the boxed regions in (B). In (C), the motility of Atg13 is not correlated with that of Sec16L, indicating that autophagosome biogenesis occurs independent of ERESs. In (D), autophagosomes are formed in the absence of ERESs. Horizontal bars, 1 μm. Vertical bars, 1 min.

Kymographs of Sec16L mobility over time showed that ERESs moved bidirectionally within a confined region (within 2–3 μm), and most did not traverse large distances (>5 μm) within the axon (Figure 6A). Kymographs also clearly displayed the decreasing gradient of ERESs from the cell soma to the distal tip, with few ERESs in the axon terminal. The same gradient was observed with another ERES marker, Sec24D (data not shown). These observed gradients along the axon are consistent with the cell soma being the primary site of protein synthesis in primary neurons.

The limited presence of ERESs in the distal axon suggests that autophagosomes may not arise from ERESs, which we confirmed by dual-color live-cell imaging of Atg13 and Sec16L (Figures 6B–6D). In the event that an autophagosome was formed near an ERES, kymograph analysis showed that their motility was neither correlated nor overlapping (Figures 6B and 6C). Thus, the ERESs and nascent autophagosomes are distinct structures, and autophagosomes are not generated from ERESs in primary neurons.

Next, we asked whether autophagosomes formed at double FYVE-containing protein 1 (DFCP1)-positive subdomains of the ER. DFCP1 is an ER-localized PI(3)P-binding protein that in mammalian cells is thought to create a platform structure (the omegasome) from which the isolation membrane will nucleate

from the ER (Axe et al., 2008). We imaged only those neurons expressing low levels of DFCP1. Consistent with previous reports (Axe et al., 2008), in DRG neurons, DFCP1 initially appears as a punctum that grows into a ring seen as a flattened disc as it rotates (Figure 7A). The ring structure created with DFCP1 is a true ring unlike that of the autophagosome, which is a closed spherical organelle that only appears as a ring due to confocal optical sectioning of this large organelle. The DFCP1 ring then collapses rather dramatically with a lifetime of ~6 min (Figure 7A). The progressive increase in diameter and intensity followed by collapse can also clearly be seen with kymograph analysis (Figure 7A).

We found that neuronal autophagosomes originate from DFCP1-labeled regions of the ER. We observed an ordered recruitment of these factors in the assembly of the nascent autophagosome. Atg13 appearance was followed by recruitment of DFCP1, and Atg13 disassembled prior to collapse of the DFCP1 ring (Figure 7B; Movie S3). In contrast to the precise colocalization observed between Atg13 and LC3 puncta, Atg13 puncta appeared either inside or beside the DFCP1 ring (Figure 7B; Movie S3). Kymograph analysis showed comigration between Atg13 and DFCP1, indicating that these structures are associated during autophagosome formation (Figure 7C). Thus, autophagosome biogenesis in primary neurons utilizes DFCP1-positive subdomains of the ER onto which assembly factors are recruited and disassembled in an ordered fashion.

We observed an enrichment of autophagosome biogenesis events in the distal axon (Figure 2), so we determined the distribution of DFCP1-positive biogenesis events within the neuron. Movies were obtained from the cell body, midaxon, and distal axon tip of the same neuron, and the number of DFCP1 biogenesis events in each domain was quantitated. DFCP1 biogenesis events were enriched in the distal tip of the axon, whereas DFCP1 biogenesis events in the cell soma and axon were infrequent (Figure 7D). Thus, consistent with the spatially regulated autophagosome biogenesis we observed (Figure 2), the distribution of DFCP1-positive ER structures is also enriched in the distal axon.

DISCUSSION

Using live-cell imaging, we investigated the spatiotemporal dynamics of autophagosome assembly in primary neurons in vitro under basal growth conditions. We find that autophagosome formation in primary neurons involves a highly ordered pathway that proceeds with stereotypical kinetics. In DRG neurons, new autophagosomes are continuously generated at a rate of ~0.6 per min; formation of a single autophagosome takes 4–6 min. Hippocampal neurons also exhibit robust biogenesis of constitutive autophagosomes, albeit at an ~4-fold slower rate. We find that neuronal autophagosomes originate from specialized subdomains of the ER marked by the formation of DFCP1-positive ring structures. Remarkably, autophagosome biogenesis in primary neurons is spatially regulated along the axon. Although autophagosomes can form in the cell soma and midaxon, >80% of biogenesis occurs at the distal axon tip. This spatial specificity echoes the DFCP1 gradient observed along the axon. Importantly, the spatial regulation observed in DRG neurons was also observed in hippocampal neurons, including cultures establishing synaptic connections.

Consistent with previous studies in nonpolarized cells by Itakura and Mizushima (2010), Koyama-Honda et al. (2013), and Suzuki et al. (2001, 2007), we observed an ordered recruitment of Atg13 and Atg5 followed by LC3 onto nascent autophagosomes (Figure 7E). We note that Atg13 and Atg5 recruitment occurs almost simultaneously within the time resolution of our experiment (one frame every 2 s) (Figure 7E). Atg13 puncta appear prior to DFCP1, and by extension, Atg5 is recruited prior to DFCP1. Appearance of Atg5 simultaneously with Atg13 and upstream of DFCP1 is unexpected considering that genetic studies have functionally ordered Atg5 downstream of both Atg13 and DFCP1 (Itakura and Mizushima, 2010). These results suggest that either these proteins localize to the autophagosome assembly site prior to their function or that the biochemical reaction rates exceed our imaging resolution. Although Atg13 and Atg5 arrive at the nascent autophagosome at the same time, Atg5 disassembles from the nascent autophagosome prior to loss of Atg13 (Figure 7E). DFCP1 exit follows Atg13 decay.

These events proceed with stereotypical kinetics. Atg13 and Atg5 have an average lifetime of ~3.3 and ~3.0 min, respectively, on the nascent autophagosome, peaking ~1.3 and ~1.0 min, respectively, after initial appearance. LC3 initially undergoes a lag phase, followed by a robust rise to maximum intensity within 1.5 min. By the time LC3 reaches peak intensity, Atg5 has already begun a sharp decay. Thus, the formation of autophagosomes in primary neurons involves a highly ordered assembly and disassembly of proteins at the nucleation site.

The source of autophagosome membrane has been the subject of contentious debate. Autophagosomes could form de novo from newly synthesized lipids, or they could arise from preexisting organelles. We find that nascent autophagosomes are associated with the ER in the distal axon as evidenced by Atg13 colocalization and comigration with the ER marker Sec61β. Furthermore, Atg13 puncta overlapped with DFCP1-positive subdomains of the ER. Our results support a model in which the ER supplies membrane to developing autophagosomes under basal conditions in primary neurons (Figure 7E). Our data are in agreement with both electron tomography (Hayashi-Nishino et al., 2009; Ylä-Anttila et al., 2009) and colocalization studies (Axe et al., 2008; Itakura and Mizushima, 2010) implicating ER as the primary source for autophagosome membrane in other cell types. Activated Ulk1 complex is thought to be recruited to the ER along with the PI(3)P kinase complex, leading to local production of PI(3)P (Itakura and Mizushima, 2010; Matsunaga et al., 2010; Mizushima et al., 2011; Weidberg et al., 2011). DFCP1 is then recruited to P1(3)P-enriched domains and organizes a platform structure (the omegasome) at the ER from which the isolation membrane will be nucleated (Axe et al., 2008). 3D electron tomography provides strong evidence that the ER forms a cradle around and is connected to the isolation membrane during autophagosome formation (Hayashi-Nishino et al., 2009; Ylä-Anttila et al., 2009).

By contrast, other reports have implicated the plasma membrane (Hollenbeck, 1993; Ravikumar et al., 2010), mitochondria (Hailey et al., 2010), ER-mitochondrial contact sites (Hamasaki et al., 2013), ERESs (Graef et al., 2013), the ER-Golgi intermediate compartment (Ge et al., 2013), the Golgi (van der Vaart and Reggiori, 2010), and recycling endosomes (Longatti et al., 2012; Puri et al., 2013) in autophagosome formation. Many of

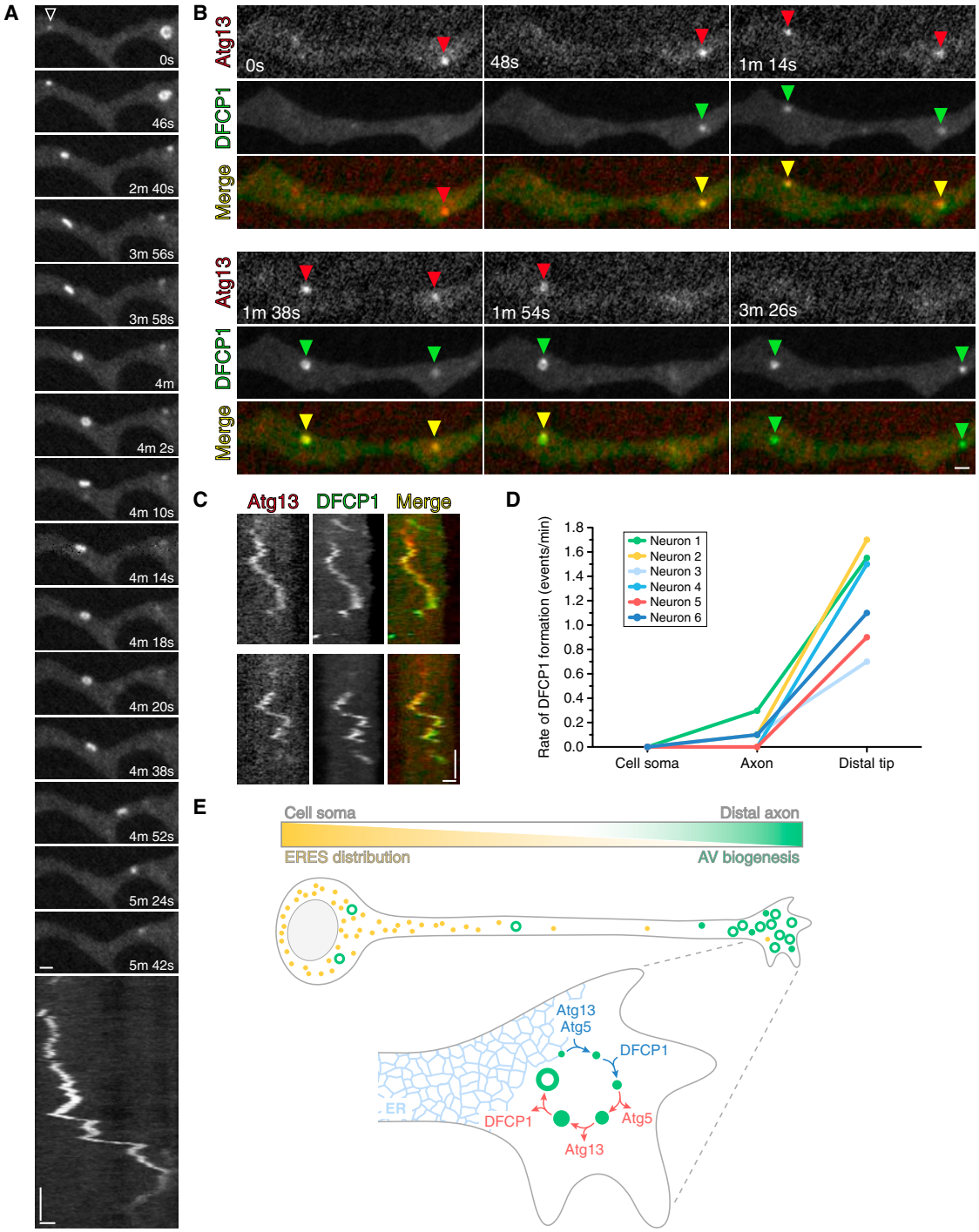

Figure 7. Neuronal Autophagosomes Form at DFCP1-Positive Subdomains of the ER

(A) Time series and corresponding kymograph of the assembly and disassembly of a GFP-DFCP1-positive structure (arrowhead) in the distal axon of a DRG neuron. The retrograde direction is toward the right. Horizontal bars, 1 μm. Vertical bar, 1 min.

(B) Time series of mCherry-Atg13 and GFP-DFCP1 in the distal axon. Red and green arrowheads denote the ordered assembly of Atg13 followed by DFCP1 and ordered disassembly of Atg13 followed by DFCP1. The duration of overlap between these two markers is denoted with yellow arrowheads. The retrograde direction is toward the right. Scale bar, 1 μm. See also Movie S3.

(C) Kymographs generated from the movie in (B) show colocalization and comigration between Atg13 and DFCP1. Horizontal bar, 1 μm. Vertical bar, 1 min.

(D) Paired plot of DFCP1 biogenesis rates in the cell body, axon, and distal tip from the same neuron showing an increasing gradient of DFCP1 structures from cell soma to distal tip (n = 6 neurons from two separate experiments). Movies were obtained for 10 min in each region. Only neurons with low DFCP1 expression were measured as overexpression of DFCP1 lead to uncoupling of the gradient.

(E) Model for autophagosome formation in primary neurons.

these studies were performed under stress-induced nutrient deprivation, suggesting that there may be differential membrane sources for constitutive versus stress-induced autophagy. During metabolic stress, autophagy may be less discriminating in its membrane derivation and source lipid from various organelles.

Membrane origin may also be cell-type specific. In a yeast cell 5 μm wide, the Golgi may provide membrane for autophagosomes because they form in close proximity. However, in primary neurons, the spatial landscape is dramatically different. The Golgi is concentrated in the cell soma and thus unlikely to provide membrane for autophagosomes generated at the distal axon, at distances that can reach up to 1,000 μm away.

Our most striking observation is the spatial regulation of autophagosome biogenesis in primary neurons. Autophagosomes were present throughout the neuron, along the axon, in the cell body, and dendrites (and see Bunge, 1973; Hernandez et al., 2012; Lee et al., 2011; Maday et al., 2012; Yue, 2007). However, autophagosome formation preferentially occurred in the distal tip of the axon; few were generated along the midaxon or in the cell soma (Figure 7E). The distal enrichment of autophagosome biogenesis observed in developing DRG neurons was paralleled in synaptically connected hippocampal neurons, albeit the rates of distal formation in hippocampal neurons were lower than those observed in actively growing DRG neurons. Because flux along the midaxon was remarkably similar between these neuronal subtypes, the difference in biogenesis rates suggests that autophagosome formation in synaptically connected hippocampal neurons may not be as tightly restricted to the distal axon as in developing DRG neurons. Although there may be higher levels of formation of autophagosomes along the midaxon of hippocampal neurons, low biogenesis rates distributed over the cumulative distance of the axon make observing these events rare.

This spatial regulation indicates a high degree of compartmentalization within the neuron. ERESs are concentrated in the cell soma with few in the distal axon. Both DFCP1 and autophagosome biogenesis are enriched distally (Figure 7E). Thus, there are opposing gradients along the axon, emphasizing the striking ability of neurons to compartmentalize functions. Although local translation has been observed in the distal axon (Holt and Schuman, 2013), the bulk of protein synthesis occurs in the cell soma. However, >80% of autophagosome formation occurs distally. The enrichment of DFCP1-positive structures in the distal tip suggests that perhaps the ER in the distal axon is more specialized and primed for autophagosome production. Alternatively, autophagy regulators such as mammalian target of rapamycin may also share a polarized distribution or activity along the axon, accounting for this distal enrichment of autophagosome formation. Compartmentalization within the neuron is further evident from our observations that autophagosome dynamics in dendrites are distinct from those in axons. These differences may result from the underlying mixed polarity of dendritic microtubules as compared to the unipolar organization of axonal microtubules or may reflect differential regulation; future work will be needed to explore these possibilities.

Our results raise an interesting question as to why autophagosomes are preferentially generated at the distal end of the axon. The axon terminal is a region rich in activity because it is actively remodeled during phases of extension and retraction during neurite outgrowth. As a result, there is an increased demand for membrane recycling, and organelles in this region might be more susceptible to damage. Electron microscopy studies have shown autophagosomes in various stages of development to be enriched in growth cones, particularly in regions undergoing retraction (Bunge, 1973). However, our observations in hippocampal neurons also demonstrate the distal enrichment of autophagosome formation, suggesting that this spatial regulation is not limited to DRG neurons actively extending processes. Thus, constitutive autophagy in the distal axon may act to counterbalance the anterograde flow of slow axonal transport. Cytoplasmic proteins synthesized in the cell soma reach the distal axon in a slow sustained stream that moves 1–10 mm per day (Brown, 2000; Scott et al., 2011). In a human motor neuron 1 m in length, cytoplasmic proteins transported by slow transport would have aged from ~100 days up to 2.7 years upon arrival in the distal tip. How these long-lived proteins are degraded or recycled once they reach the axon terminal is unclear. High autophagic activity in the distal axon may serve to counteract the distal accumulation of aged proteins over time.

Elevated levels of autophagy in the distal axon may also be required to recycle aged organelles that preferentially distribute to the distal axon. Mitochondria residing in the distal axon are older than those residing proximal to the cell soma (Ferree et al., 2013). Located further from primary sites of protein synthesis, organelles in the distal axon may be more susceptible to aging and damage because their proteins are less efficiently replenished. Consistent with this idea, higher levels of mtDNA damage have been detected in distal axons in patients with HIV-related sensory neuropathy (Lehmann et al., 2011). Thus, elevated autophagy in the distal axon may provide a mechanism to recycle aged and damaged mitochondria in the distal region of long axons.

Although autophagosome biogenesis can occur in the midaxon or cell soma, these events are infrequent under basal conditions. So how are damaged organelles and proteins along the midaxon cleared? Perhaps the axon has a limited capacity for degradation. A striking feature that unifies many neurodegenerative diseases is the aberrant accumulation of protein aggregates along the axon that results in axonal retraction. The autophagic pathway is preferentially elevated in the distal axon in some disease models. For example, in a mouse model of excitotoxic neurodegeneration, autophagosomes preferentially accumulate in the distal axons of Purkinje neurons, at levels exceeding those in the cell soma or dendrites (Wang et al., 2006). A Purkinje cell-specific knockout of Atg7 is sufficient to cause degeneration of the axon terminal with little effect on dendrites, indicating a critical role for autophagy in the maintenance of axon terminals (Komatsu et al., 2007). Furthermore, neocortical biopsies from Alzheimer's disease brain exhibit a pronounced accumulation of autophagosomes in the axons as compared to the soma, with particular abundance in synaptic terminals (Nixon et al., 2005). Collectively, these data emphasize a role for the compartmentalized regulation of autophagy but suggest that beyond a certain threshold, the autophagic system is unable to effectively remove damaged proteins or dysfunctional organelles, rendering the neuron susceptible to disease.

Autophagy has also been linked to synaptic structure and function. Autophagy regulates presynaptic activity and vesicle

release, neuromuscular junction structure, as well as receptor turnover in the postsynaptic membrane (Hernandez et al., 2012; Shehata et al., 2012; Shen and Ganetzky, 2009). In developing DRG neurons that do not form synapses, autophagosome formation was significantly enriched in the distal axon, perhaps due to the dynamic states of growth cone extension and retraction. In contrast, in synaptically connected hippocampal neurons, constitutive autophagosome biogenesis is less tightly restricted to the distal axon, potentially occurring at en passant synapses along the midaxon as suggested by observations in dopaminergic neurons (Hernandez et al., 2012). Future work is required to address the possibility that stimulation of synaptic activity alters dynamics and increases autophagosome formation along the midaxon. Furthermore, examination of autophagosome formation and dynamics in vivo will provide additional insights on the regulation of autophagy in developing versus mature systems undergoing physiological levels of synaptic activity.

Together, our results highlight the high degree of compartmentalization and spatial regulation imposed on cellular pathways within the neuron. We find that autophagosome biogenesis in primary neurons is a polarized process that is spatiotemporally regulated along the axon. Our findings here provide insights into the unique vulnerability of neurons to increased protein aggregation along the axon, resulting in neuronal dysfunction and degeneration.

EXPERIMENTAL PROCEDURES

Reagents

GFP-LC3 transgenic mice, strain name B6.Cg-Tg(CAG-EGFP/LC3)53Nmi/NmiRbrc (Mizushima et al., 2004), were obtained from the RIKEN BioResource Center in Japan. Constructs and antibodies are detailed in the Supplemental Experimental Procedures.

Imaging of Primary Neurons

Primary Neuron Culture

DRG neurons were cultured as previously described (Maday et al., 2012); see Supplemental Experimental Procedures for details. For hippocampal neurons, the hippocampus was dissected from embryonic day 15.5 mice of either sex, dissociated in 0.25% trypsin, and triturated through a Pasteur pipet, as described in the Supplemental Experimental Procedures. To determine the directionality of single axons during live-cell imaging, GFP-LC3-positive neurons were diluted 1:10 with GFP-LC3-negative neurons isolated from nontransgenic littermates. With this dilution, single GFP-LC3-positive neurons could be observed, and the directionality of the axon was determined based on criteria established by Kaech and Banker (2006). All animal protocols were approved by the Institutional Animal Care and Use Committee at the University of Pennsylvania.

Live-Cell Imaging

Live-cell imaging was performed as described in Maday et al. (2012); see the Supplemental Experimental Procedures. Biogenesis movies from the mid and distal axon were obtained whenever possible from the same neuron. For hippocampal cultures, axons were selected for imaging based on morphologic criteria (Kaech and Banker, 2006): thin and uniform caliber with no swellings or varicosities along the length. Dendrites were also identified based on morphologic criteria (Kaech and Banker, 2006): 200–300 μm lengths that tapered with distance from the cell soma. Kymographs were generated using the Multiple Kymograph plugin in FIJI using a line width of 3 or 5.

Image Analysis

Quantitation of Biogenesis along the Axon

Quantitation of intensity profiles is described in the Supplemental Experimental Procedures. Movies were acquired within ~50 μm (for DRG neurons) or ~70 μm (for hippocampal neurons) of the distal end of the axon, defined here as the distal tip, over an ~80 μm window along the midaxon that spanned 500–1,000 μm in length (length for DRG neurons), or in the cell soma, ~25 μm in diameter. For all DFCP1 experiments, a single distal tip, midaxon, and cell soma movie was obtained from the same neuron. For the Atg13 and Atg5 experiments, some but not all movies were obtained from the same neuron. Only neurons with low Atg13 or Atg5 expression were imaged in order to observe specific events of biogenesis. Only neurons with a mean intensity of ≤6.2 arbitrary units (corrected for background) for cytosolic DFCP1 intensity were quantified. We imaged neurons with flat axon tips in order to accurately count the total number of biogenesis events in the region. Biogenesis events were defined by changes in intensity and size of Atg5, Atg13, LC3, or DFCP1 over time as measured in Figures 1 and 7A. Any biogenesis event within each domain was counted and normalized for movie duration.

Quantitation of Axonal Transport in Hippocampal Neurons

Using FIJI, kymographs (line width 3) were generated from movies along the axon >50 μm from the cell soma and >100 μm from the distal tip. For each kymograph, the percentage of autophagosomes moving in the net retrograde direction (displacement of ≥5 μm within the 5 min imaging window) versus net anterograde direction (displacement of ≥5 μm within 5 min) was determined. Vesicles that did not move a net 5 μm within the 5 min imaging window were classified as bidirectional or stationary. Flux (number of autophagosomes within 100 μm/min) was determined from each kymograph as the sum of retrograde, anterograde, and bidirectional/stationary vesicles normalized by kymograph length and time. Average velocity of retrograde autophagosomes was calculated as displacement divided by total time taken.

Quantitation of Dendritic Transport in Hippocampal Neurons

A comprehensive analysis of dendritic autophagosome motility was limited due to the increased depth of the dendrite combined with brighter microtubule labeling by GFP-LC3. Thus, only autophagosomes that could be tracked unambiguously were categorized as retrograde (processive movement in the retrograde direction; displacement of ≥5 μm), anterograde (processive movement in the anterograde direction; displacement of ≥5 μm), stationary (displacement of <5 μm), or bidirectional (processive movement of 5 μm in both anterograde and retrograde directions).

Additional Methods

All image measurements were obtained from the raw data. Procedures describing immunostain, line scans, and Pearson's correlation coefficient measurements are provided in the Supplemental Experimental Procedures. GraphPad Prism was used to plot graphs and perform statistical tests; statistical tests are denoted within each figure legend. Images were prepared in FIJI; contrast and brightness were adjusted equally to all images within a series. Figures were assembled in Adobe Illustrator.

SUPPLEMENTAL INFORMATION

Supplemental Information includes Supplemental Experimental Procedures, four figures, and three movies and can be found with this article online at http://dx.doi.org/10.1016/j.devcel.2014.06.001.

AUTHOR CONTRIBUTIONS

S.M. and E.L.F.H. designed experiments. S.M. performed experiments. S.M. and E.L.F.H. analyzed data. S.M. and E.L.F.H. wrote the manuscript.

ACKNOWLEDGMENTS

The authors gratefully acknowledge the technical assistance of Mariko Tokito and Karen Jahn. We thank Swathi Ayloo, Alison Twelvetrees, Meredith Wilson, and Adam Hendricks for helpful discussion. The authors also thank Allison Zajac for the MATLAB script for color-coding tracks. This work was funded by NIH grant K99NS082619 to S.M. and NIH grant NS060698 to E.L.F.H.

Received: October 18, 2013
Revised: April 8, 2014
Accepted: May 30, 2014
Published: July 14, 2014

REFERENCES

Axe, E.L., Walker, S.A., Manifava, M., Chandra, P., Roderick, H.L., Habermann, A., Griffiths, G., and Ktistakis, N.T. (2008). Autophagosome formation from membrane compartments enriched in phosphatidylinositol 3-phosphate and dynamically connected to the endoplasmic reticulum. J. Cell Biol. *182*, 685–701.

Baas, P.W., Deitch, J.S., Black, M.M., and Banker, G.A. (1988). Polarity orientation of microtubules in hippocampal neurons: uniformity in the axon and nonuniformity in the dendrite. Proc. Natl. Acad. Sci. USA *85*, 8335–8339.

Bhattacharyya, D., and Glick, B.S. (2007). Two mammalian Sec16 homologues have nonredundant functions in endoplasmic reticulum (ER) export and transitional ER organization. Mol. Biol. Cell *18*, 839–849.

Brown, A. (2000). Slow axonal transport: stop and go traffic in the axon. Nat. Rev. Mol. Cell Biol. *1*, 153–156.

Bunge, M.B. (1973). Fine structure of nerve fibers and growth cones of isolated sympathetic neurons in culture. J. Cell Biol. *56*, 713–735.

Ferree, A.W., Trudeau, K., Zik, E., Benador, I.Y., Twig, G., Gottlieb, R.A., and Shirihai, O.S. (2013). MitoTimer probe reveals the impact of autophagy, fusion, and motility on subcellular distribution of young and old mitochondrial protein and on relative mitochondrial protein age. Autophagy *9*, 1887–1896.

Ge, L., Melville, D., Zhang, M., and Schekman, R. (2013). The ER-Golgi intermediate compartment is a key membrane source for the LC3 lipidation step of autophagosome biogenesis. eLife *2*, e00947.

Graef, M., Friedman, J.R., Graham, C., Babu, M., and Nunnari, J. (2013). ER exit sites are physical and functional core autophagosome biogenesis components. Mol. Biol. Cell *24*, 2918–2931.

Hailey, D.W., Rambold, A.S., Satpute-Krishnan, P., Mitra, K., Sougrat, R., Kim, P.K., and Lippincott-Schwartz, J. (2010). Mitochondria supply membranes for autophagosome biogenesis during starvation. Cell *141*, 656–667.

Hamasaki, M., Furuta, N., Matsuda, A., Nezu, A., Yamamoto, A., Fujita, N., Oomori, H., Noda, T., Haraguchi, T., Hiraoka, Y., et al. (2013). Autophagosomes form at ER-mitochondria contact sites. Nature *495*, 389–393.

Hara, T., Nakamura, K., Matsui, M., Yamamoto, A., Nakahara, Y., Suzuki-Migishima, R., Yokoyama, M., Mishima, K., Saito, I., Okano, H., and Mizushima, N. (2006). Suppression of basal autophagy in neural cells causes neurodegenerative disease in mice. Nature *441*, 885–889.

Harding, T.M., Morano, K.A., Scott, S.V., and Klionsky, D.J. (1995). Isolation and characterization of yeast mutants in the cytoplasm to vacuole protein targeting pathway. J. Cell Biol. *131*, 591–602.

Hayashi-Nishino, M., Fujita, N., Noda, T., Yamaguchi, A., Yoshimori, T., and Yamamoto, A. (2009). A subdomain of the endoplasmic reticulum forms a cradle for autophagosome formation. Nature Cell Biol. *11*, 1433–1437.

Hernandez, D., Torres, C.A., Setlik, W., Cebrián, C., Mosharov, E.V., Tang, G., Cheng, H.C., Kholodilov, N., Yarygina, O., Burke, R.E., et al. (2012). Regulation of presynaptic neurotransmission by macroautophagy. Neuron *74*, 277–284.

Hollenbeck, P.J. (1993). Products of endocytosis and autophagy are retrieved from axons by regulated retrograde organelle transport. J. Cell Biol. *121*, 305–315.

Holt, C.E., and Schuman, E.M. (2013). The central dogma decentralized: new perspectives on RNA function and local translation in neurons. Neuron *80*, 648–657.

Itakura, E., and Mizushima, N. (2010). Characterization of autophagosome formation site by a hierarchical analysis of mammalian Atg proteins. Autophagy *6*, 764–776.

Kaech, S., and Banker, G. (2006). Culturing hippocampal neurons. Nat. Protoc. *1*, 2406–2415.

Kitada, T., Asakawa, S., Hattori, N., Matsumine, H., Yamamura, Y., Minoshima, S., Yokochi, M., Mizuno, Y., and Shimizu, N. (1998). Mutations in the parkin gene cause autosomal recessive juvenile parkinsonism. Nature *392*, 605–608.

Klionsky, D.J., Cregg, J.M., Dunn, W.A., Jr., Emr, S.D., Sakai, Y., Sandoval, I.V., Sibirny, A., Subramani, S., Thumm, M., Veenhuis, M., and Ohsumi, Y. (2003). A unified nomenclature for yeast autophagy-related genes. Dev. Cell *5*, 539–545.

Komatsu, M., Waguri, S., Chiba, T., Murata, S., Iwata, J., Tanida, I., Ueno, T., Koike, M., Uchiyama, Y., Kominami, E., and Tanaka, K. (2006). Loss of autophagy in the central nervous system causes neurodegeneration in mice. Nature *441*, 880–884.

Komatsu, M., Wang, Q.J., Holstein, G.R., Friedrich, V.L., Jr., Iwata, J., Kominami, E., Chait, B.T., Tanaka, K., and Yue, Z. (2007). Essential role for autophagy protein Atg7 in the maintenance of axonal homeostasis and the prevention of axonal degeneration. Proc. Natl. Acad. Sci. USA *104*, 14489–14494.

Koyama-Honda, I., Itakura, E., Fujiwara, T.K., and Mizushima, N. (2013). Temporal analysis of recruitment of mammalian ATG proteins to the autophagosome formation site. Autophagy *9*, 1491–1499.

Lee, S., Sato, Y., and Nixon, R.A. (2011). Lysosomal proteolysis inhibition selectively disrupts axonal transport of degradative organelles and causes an Alzheimer's-like axonal dystrophy. J. Neurosci. *31*, 7817–7830.

Lehmann, H.C., Chen, W., Borzan, J., Mankowski, J.L., and Höke, A. (2011). Mitochondrial dysfunction in distal axons contributes to human immunodeficiency virus sensory neuropathy. Ann. Neurol. *69*, 100–110.

Longatti, A., Lamb, C.A., Razi, M., Yoshimura, S., Barr, F.A., and Tooze, S.A. (2012). TBC1D14 regulates autophagosome formation via Rab11- and ULK1-positive recycling endosomes. J. Cell Biol. *197*, 659–675.

Maday, S., Wallace, K.E., and Holzbaur, E.L. (2012). Autophagosomes initiate distally and mature during transport toward the cell soma in primary neurons. J. Cell Biol. *196*, 407–417.

Mariño, G., Madeo, F., and Kroemer, G. (2011). Autophagy for tissue homeostasis and neuroprotection. Curr. Opin. Cell Biol. *23*, 198–206.

Matsunaga, K., Morita, E., Saitoh, T., Akira, S., Ktistakis, N.T., Izumi, T., Noda, T., and Yoshimori, T. (2010). Autophagy requires endoplasmic reticulum targeting of the PI3-kinase complex via Atg14L. J. Cell Biol. *190*, 511–521.

Millecamps, S., and Julien, J.P. (2013). Axonal transport deficits and neurodegenerative diseases. Nat. Rev. Neurosci. *14*, 161–176.

Mizushima, N., Yamamoto, A., Hatano, M., Kobayashi, Y., Kabeya, Y., Suzuki, K., Tokuhisa, T., Ohsumi, Y., and Yoshimori, T. (2001). Dissection of autophagosome formation using Apg5-deficient mouse embryonic stem cells. J. Cell Biol. *152*, 657–668.

Mizushima, N., Yamamoto, A., Matsui, M., Yoshimori, T., and Ohsumi, Y. (2004). In vivo analysis of autophagy in response to nutrient starvation using transgenic mice expressing a fluorescent autophagosome marker. Mol. Biol. Cell *15*, 1101–1111.

Mizushima, N., Yoshimori, T., and Ohsumi, Y. (2011). The role of Atg proteins in autophagosome formation. Annu. Rev. Cell Dev. Biol. *27*, 107–132.

Narendra, D., Tanaka, A., Suen, D.F., and Youle, R.J. (2008). Parkin is recruited selectively to impaired mitochondria and promotes their autophagy. J. Cell Biol. *183*, 795–803.

Narendra, D.P., Jin, S.M., Tanaka, A., Suen, D.F., Gautier, C.A., Shen, J., Cookson, M.R., and Youle, R.J. (2010). PINK1 is selectively stabilized on impaired mitochondria to activate Parkin. PLoS Biol. *8*, e1000298.

Nixon, R.A., Wegiel, J., Kumar, A., Yu, W.H., Peterhoff, C., Cataldo, A., and Cuervo, A.M. (2005). Extensive involvement of autophagy in Alzheimer disease: an immuno-electron microscopy study. J. Neuropathol. Exp. Neurol. *64*, 113–122.

Perlson, E., Maday, S., Fu, M.M., Moughamian, A.J., and Holzbaur, E.L. (2010). Retrograde axonal transport: pathways to cell death? Trends Neurosci. *33*, 335–344.

Puri, C., Renna, M., Bento, C.F., Moreau, K., and Rubinsztein, D.C. (2013). Diverse autophagosome membrane sources coalesce in recycling endosomes. Cell *154*, 1285–1299.

Ravikumar, B., Moreau, K., Jahreiss, L., Puri, C., and Rubinsztein, D.C. (2010). Plasma membrane contributes to the formation of pre-autophagosomal structures. Nat. Cell Biol. *12*, 747–757.

Rubinsztein, D.C., DiFiglia, M., Heintz, N., Nixon, R.A., Qin, Z.H., Ravikumar, B., Stefanis, L., and Tolkovsky, A. (2005). Autophagy and its possible roles in nervous system diseases, damage and repair. Autophagy *1*, 11–22.

Scott, D.A., Das, U., Tang, Y., and Roy, S. (2011). Mechanistic logic underlying the axonal transport of cytosolic proteins. Neuron *70*, 441–454.

Shehata, M., Matsumura, H., Okubo-Suzuki, R., Ohkawa, N., and Inokuchi, K. (2012). Neuronal stimulation induces autophagy in hippocampal neurons that is involved in AMPA receptor degradation after chemical long-term depression. J. Neurosci. *32*, 10413–10422.

Shen, W., and Ganetzky, B. (2009). Autophagy promotes synapse development in *Drosophila*. J. Cell Biol. *187*, 71–79.

Suzuki, K., Kirisako, T., Kamada, Y., Mizushima, N., Noda, T., and Ohsumi, Y. (2001). The pre-autophagosomal structure organized by concerted functions of APG genes is essential for autophagosome formation. EMBO J. *20*, 5971–5981.

Suzuki, K., Kubota, Y., Sekito, T., and Ohsumi, Y. (2007). Hierarchy of Atg proteins in pre-autophagosomal structure organization. Genes Cells *12*, 209–218.

Thumm, M., Egner, R., Koch, B., Schlumpberger, M., Straub, M., Veenhuis, M., and Wolf, D.H. (1994). Isolation of autophagocytosis mutants of Saccharomyces cerevisiae. FEBS Lett. *349*, 275–280.

Tsukada, M., and Ohsumi, Y. (1993). Isolation and characterization of autophagy-defective mutants of Saccharomyces cerevisiae. FEBS Lett. *333*, 169–174.

Valente, E.M., Abou-Sleiman, P.M., Caputo, V., Muqit, M.M., Harvey, K., Gispert, S., Ali, Z., Del Turco, D., Bentivoglio, A.R., Healy, D.G., et al. (2004). Hereditary early-onset Parkinson's disease caused by mutations in PINK1. Science *304*, 1158–1160.

van der Vaart, A., and Reggiori, F. (2010). The Golgi complex as a source for yeast autophagosomal membranes. Autophagy *6*, 800–801.

Wang, Q.J., Ding, Y., Kohtz, D.S., Mizushima, N., Cristea, I.M., Rout, M.P., Chait, B.T., Zhong, Y., Heintz, N., and Yue, Z. (2006). Induction of autophagy in axonal dystrophy and degeneration. J. Neurosci. *26*, 8057–8068.

Weidberg, H., Shvets, E., and Elazar, Z. (2011). Biogenesis and cargo selectivity of autophagosomes. Annu. Rev. Biochem. *80*, 125–156.

Xie, Z., and Klionsky, D.J. (2007). Autophagosome formation: core machinery and adaptations. Nat. Cell Biol. *9*, 1102–1109.

Ylä-Anttila, P., Vihinen, H., Jokitalo, E., and Eskelinen, E.L. (2009). 3D tomography reveals connections between the phagophore and endoplasmic reticulum. Autophagy *5*, 1180–1185.

Yue, Z. (2007). Regulation of neuronal autophagy in axon: implication of autophagy in axonal function and dysfunction/degeneration. Autophagy *3*, 139–141.

Developmental Cell, Volume *30*

Supplemental Information

Autophagosome Biogenesis in Primary Neurons Follows an Ordered and Spatially Regulated Pathway

Sandra Maday and Erika L.F. Holzbaur

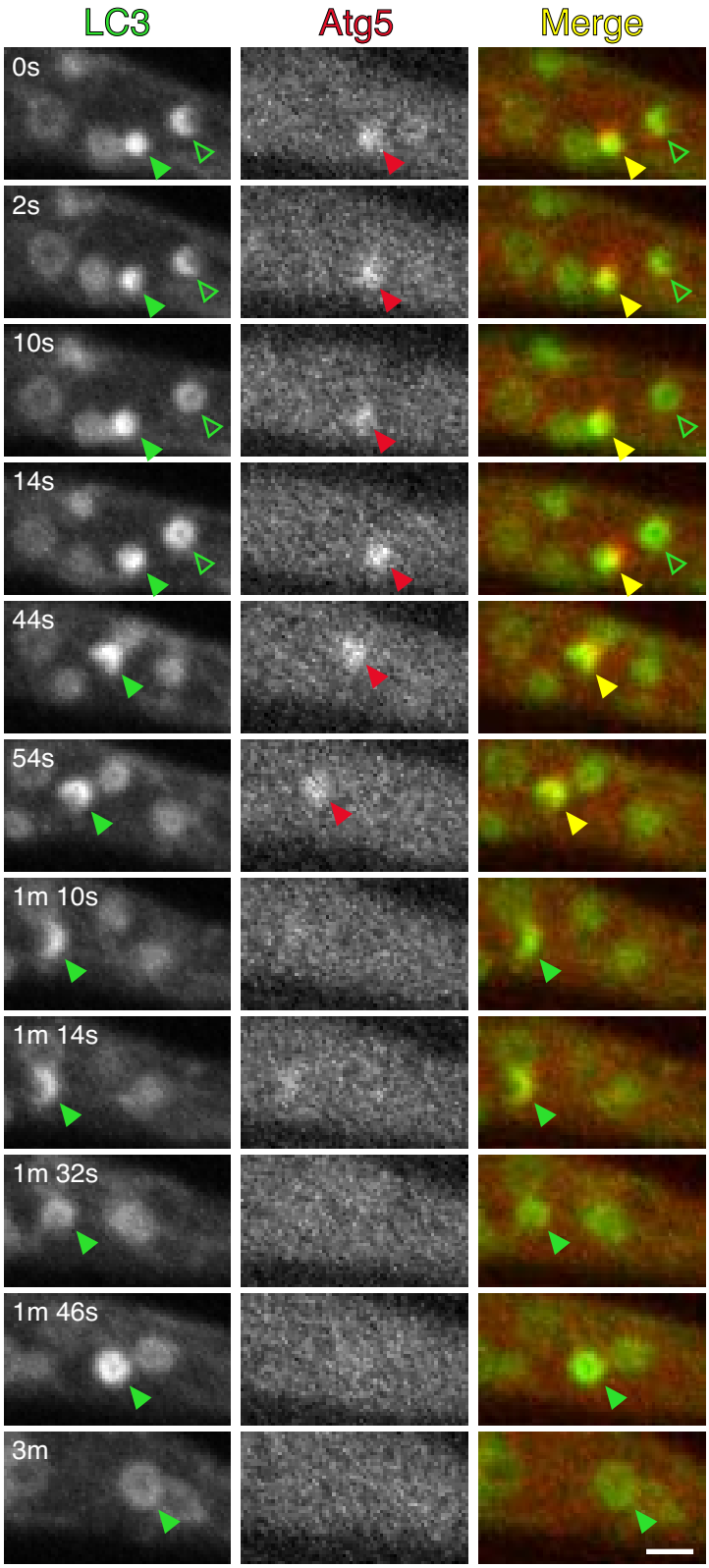

Supplementary Figure 1. Maday and Holzbaur

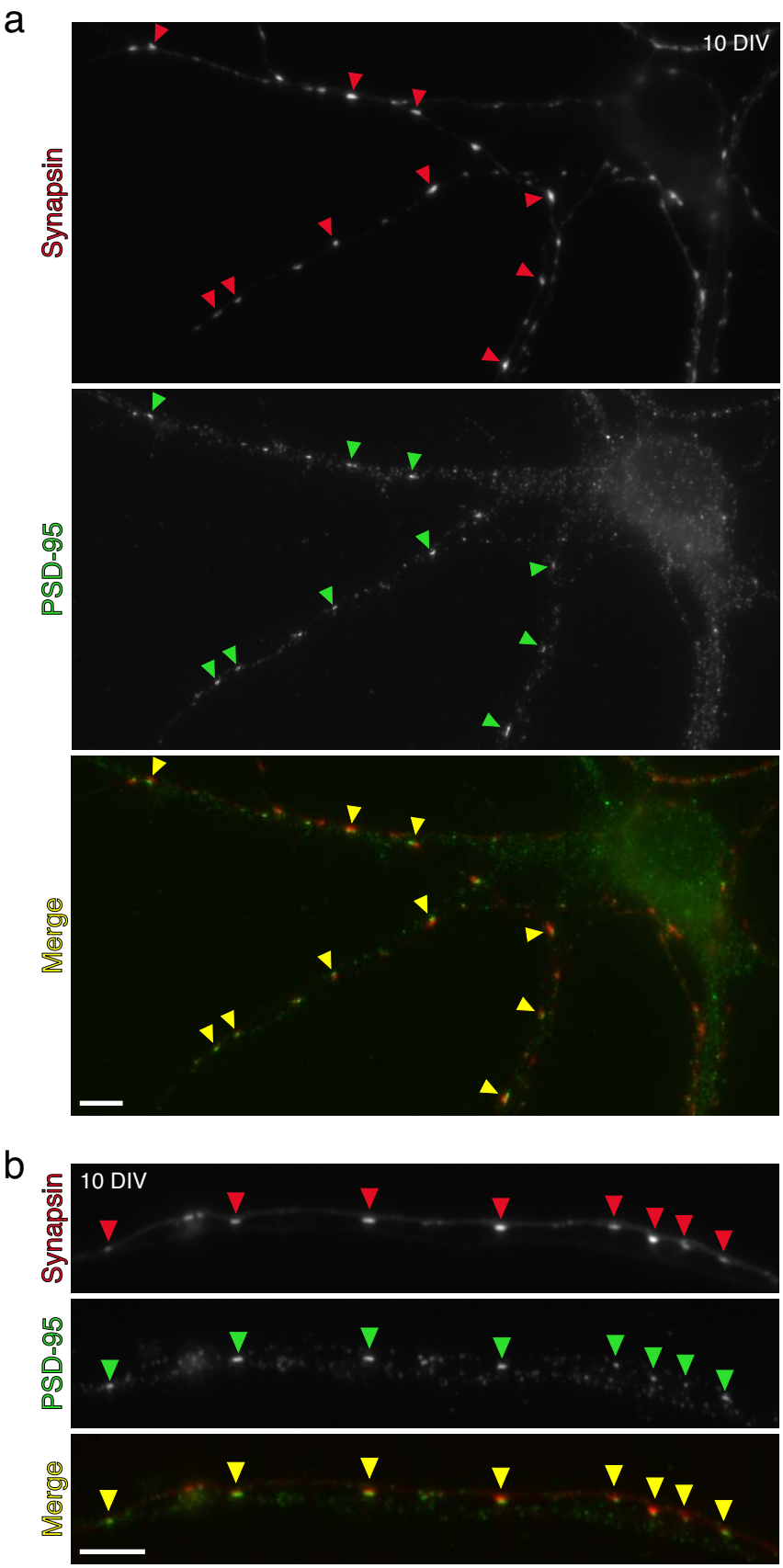

Supplementary Figure 2. Maday and Holzbaur

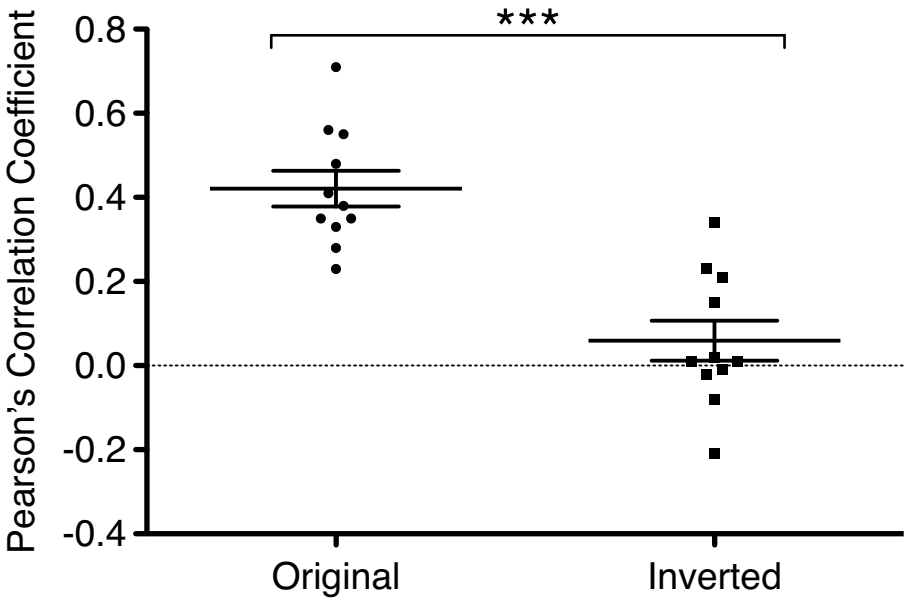

Supplementary Figure 3. Maday and Holzbaur

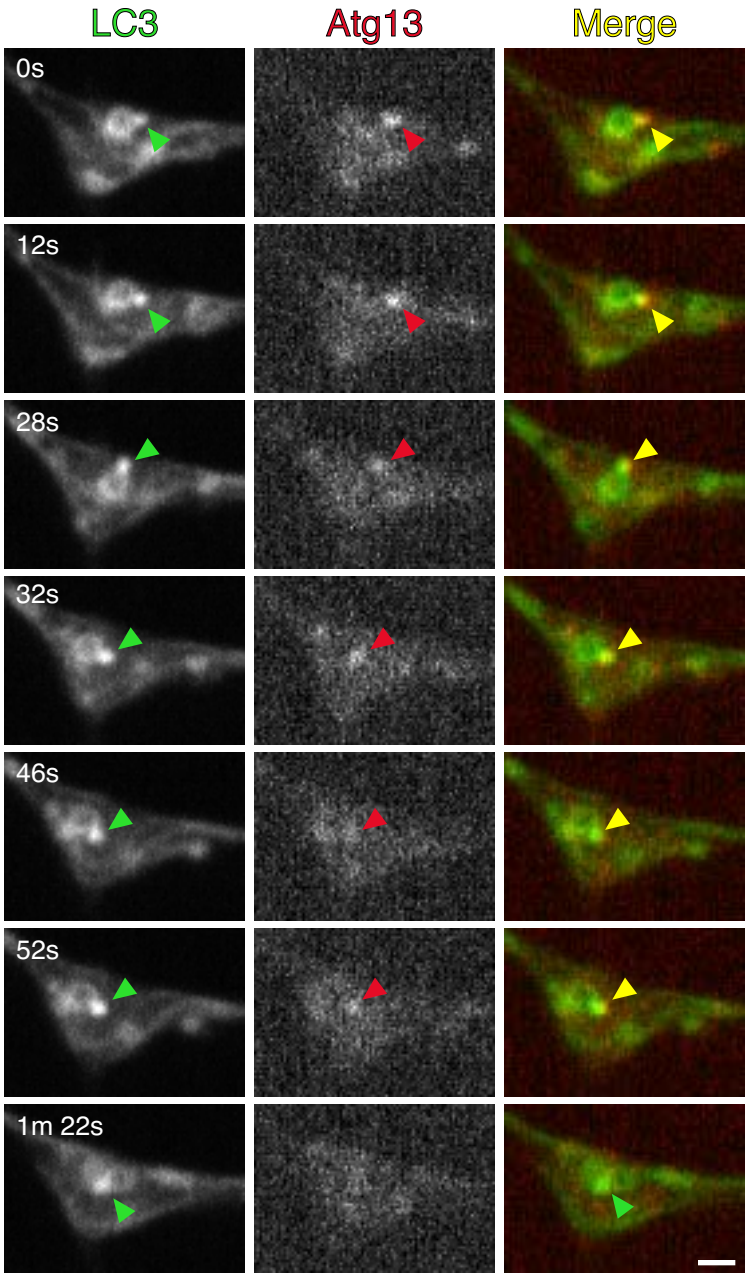

Supplementary Figure 4. Maday and Holzbaur

Supplemental Legends

Supplementary Figure 1. Occasional LC3-positive cup-shaped structures observed during autophagosome formation, related to Figure 1. Time series of GFP-LC3 and mCherry-Atg5 in the distal neurite tip of a DRG neuron. Open and closed arrowheads designate two different biogenesis events that form LC3-positive cup-shaped structures prior to completion of the closed ring. Yellow arrowheads denote colocalization between LC3 and Atg5. The red and green signals may appear slightly offset because of delays in acquiring consecutive images, green followed by red. The retrograde direction is toward the left. Scale bar, 1 μm.

Supplementary Figure 2. Hippocampal neurons form excitatory synapses at 10 DIV, related to Figure 3. (A, B) Two examples showing excitatory synapses in hippocampal neurons stained with synapsin (pre-synaptic marker) and PSD-95 (post-synaptic excitatory marker). Arrowheads denote excitatory synapses. The retrograde direction is toward the right. Scale bars, 5 μm.

Supplementary Figure 3. Colocalization between Atg13 and the ER is specific, related to Figure 5C. For kymographs of Atg13 and Sec61β that showed a positive Pearson's Correlation Coefficient (Fig. 5C), the Sec61β kymograph was flipped horizontally to measure the Pearson's Correlation Coefficient between Atg13 and the inverted ER kymograph. Shown is a scatter plot of the Pearson's Correlation Coefficient of the original and inverted kymographs (mean ± SEM; ***, $p<0.001$; paired t-test).

Supplementary Figure 4. Nascent autophagosome appears to bud from pre-existing autophagosome ring, related to Figure 5. Time series of GFP-LC3 and mCherry-Atg13 in the distal axon of DRG neurons. Green arrowheads denote a newly forming autophagosome that appears to bud from a pre-existing ring and remains attached to the ring as they move. Yellow arrowheads denote colocalization between LC3 and Atg13. The retrograde direction is toward the right. Scale bar, 1 μm.

Supplementary Movie 1. Ordered assembly of Atg5 followed by LC3 onto nascent autophagosomes, related to Figure 1B. DRG neurons isolated from transgenic mice expressing the autophagosome marker GFP-LC3 were transfected with mCherry-Atg5. The distal axon was analyzed by time-lapse confocal microscopy using a confocal spinning disk microscope (Perkin Elmer Ultra*VIEW* Vox Spinning Disk Confocal with a Nikon Eclipse Ti Microscope). Frames were taken once every 2 seconds for 11 minutes. Movie is played 20 times real time. Red and green arrowheads denote the ordered appearance of Atg5 followed by LC3, respectively in 3 separate biogenesis events. Red and green signals may appear slightly offset because of delays in acquiring consecutive images, green followed by red. The retrograde direction is toward the right. Movie stills are shown in Figure 1B.

Supplementary Movie 2. Atg13 appears on subdomains of the ER, related to Figure 5A. Wild type DRG neurons were transfected with mCherry-Atg13 and GFP-Sec61β. The distal axon was analyzed by time-lapse confocal microscopy using a confocal spinning disk microscope (Perkin Elmer Ultra*VIEW* Vox Spinning Disk Confocal with a Nikon Eclipse Ti Microscope). Frames were taken once every 2 seconds. Shown is a 2 minute imaging window. Movie is played 10 times real time. Red and green arrowheads mark colocalization between Atg13 and Sec61β, respectively. Red and green signals may appear slightly offset because of delays in acquiring consecutive images, green followed by red. The retrograde direction is toward the right. Movie stills are shown in Figure 5A.

Supplementary Movie 3. Atg13 localizes to DFCP1-positive subdomains of the ER, related to Figure 7B. Wild type DRG neurons were transfected with mCherry-Atg13 and GFP-DFCP1. The distal axon was analyzed by time-lapse confocal microscopy using a confocal spinning disk microscope (Perkin Elmer Ultra*VIEW* Vox Spinning Disk Confocal with a Nikon Eclipse Ti Microscope). Frames were taken once every 2 seconds for 10 minutes. Movie is played 20 times real time. Red and green arrowheads mark only the initial appearance of 4 separate biogenesis events, Atg13 and DFCP1 respectively. Red and green signals may appear slightly offset because of delays in acquiring consecutive images, green followed by red. The retrograde direction is toward the right. Movie stills are shown in Figure 7B.

Supplemental Experimental Procedures

Reagents

Constructs include GFP-Atg13 (Addgene #22875), mCherry-Atg5 (Addgene #13095), GFP-Sec61β (Addgene #15108), GFP-Sec16L (Addgene #15776), GFP-DFCP1 (obtained from Addgene #38269 and recloned into pEGFP-C2), Lyn-GFP (gift from Dr. Elias Spiliotis), DsRed2-mito (gift from Dr. Thomas Schwarz). The GFP tag on Atg13 was replaced with mCherry to generate mCherry-Atg13. CellMask Orange plasma membrane stain was obtained from Life Technologies. Antibodies include rabbit anti-synapsin (Cell Signaling) and mouse anti-PSD-95 (Millipore).

Imaging of primary neurons

DRG culture. Dorsal root ganglia were dissected from either GFP-LC3 transgenic (Tg/-) adult mice or non-transgenic (-/-) adult littermates 4-6 months of age of either sex, and dissociated in 20 Units/ml papain followed by 2 mg/ml collagenase type II and 2.4 mg/ml dispase II. The ganglia were then triturated and purified through 20% Percoll. Prior to plating, cells were transfected with 0.5 µg each plasmid DNA using an amaxa nucleofector (Lonza) according to manufacturer's specifications. For live-cell imaging, DRG neurons were plated onto glass-bottom dishes (World Precision Instruments, Inc.) coated with 0.1 mg/ml Poly-L-Lysine and 20 µg/ml laminin. DRG neurons were cultured for 2 days in F-12 media (Invitrogen) supplemented with 10% heat inactivated fetal bovine serum, 1 mM L-glutamine, 100 units/ml penicillin and 100 µg/ml streptomycin at 37°C in a 5% CO_2 incubator.

Hippocampal culture. 750,000 neurons were plated onto acid-washed 25 mm glass coverslips (Carolina Biosciences) coated with 500 µg/ml Poly-L-Lysine and positioned in a 10 cm culture dish. Hippocampal neurons were cultured for 5-16 days in Neurobasal medium supplemented with 2% B-27, 37.5 mM NaCl, 33 mM glucose, 2 mM GlutaMAX, and 100 units/ml penicillin and 100 µg/ml streptomycin at 37°C in a 5% CO_2 incubator. Every 3-4 days, 20-30% media was changed and 1 µM AraC was added.

Live-cell imaging. Live-cell imaging was performed in low fluorescence Hibernate A (BrainBits; for DRG neurons) or Hibernate E (BrainBits; for hippocampal neurons) supplemented with 2% B-27 and 2 mM GlutaMAX. Coverslips with hippocampal neurons were placed in a Chamlide CMB magnetic imaging chamber (BioVision Technologies). Live-cell microscopy was performed on a Perkin Elmer Ultra*VIEW* Vox Spinning Disk Confocal with a Nikon Eclipse Ti Inverted Microscope with the Perfect Focus System using an Apochromat 100X 1.49 NA oil-immersion objective (Nikon) in an environmental chamber at 37° C. Digital images were acquired with a Hamamatsu EMCCD C9100-50 camera using Volocity software (Perkin Elmer). Solid state 488 nm and 561 nm lasers (Perkin-Elmer) were used for excitation. Images in DRG neurons were taken once every 2 seconds for 5-10 minutes, green followed by red. Images in hippocampal neurons were taken once every 2 seconds for 5 minutes (axonal transport) or 10 minutes (biogenesis).

Immunostain. Hippocampal neurons grown 10 DIV were fixed in 37°C 4% PFA/4% sucrose for 10 minutes, washed two times in PBS, and permeabilized in 0.1% Triton X-100 in PBS for 5 minutes. Samples were then washed two times in PBS and blocked for 1 hour in 5% goat serum; 1% BSA in PBS. Cells were incubated in primary antibody diluted in blocking buffer for 1 hour, washed 3 times for 5 minutes each in PBS, incubated in secondary antibody diluted in blocking buffer for 1 hour, washed 3 times for 5 minutes each in PBS. Samples were then mounted in ProLong Gold (Life Technologies) and analyzed on a Leica DMI6000B inverted epifluorescence microscope using an Apochromat 63X 1.4 NA oil-immersion objective with a 1.6 optical magnification (Leica Microsystems). Digital images were acquired with a Hamamatsu ORCA-R^2 charge-coupled device camera using LAS-AF software (Leica Microsystems).

Image Analysis

Intensity profiles. All image analysis was performed in FIJI. While all particles exhibited the same pattern of ordered assembly, we quantitated only those that could be unambiguously tracked for the entire biogenesis event and were not obscured by other autophagosomes in the distal tip. For every

frame, the mean gray value for Atg13, Atg5 or LC3 was measured within the smallest circular region of interest (ROI) that would encapsulate the entire signal. The mean gray value of an ROI of exact size was used to measure the background intensity near the puncta of interest. For every frame, the corresponding background value was subtracted from the signal value. The data were smoothed by applying a mean filter of 5. The maximum intensity value from the smoothed data was used to normalize the corresponding raw data which were then expressed as a percentage. Each smoothed trace was normalized by its own maximum, expressed as a percentage and used only to determine the time at which LC3 reached half maximal signal. This time was then used to align and plot the normalized raw data traces and generate a mean. Since the five traces averaged were of varying lengths, the mean plot was truncated on either end so the mean was generated from at least 2 traces. The Atg13/LC3 and Atg5/LC3 traces were aligned on a single graph using the half maximum of LC3. The values for timing events reported in the text were obtained from the mean intensity profiles of Atg13, Atg5 and LC3. Along with intensity measurements, coordinates for the centroid of the Atg5 ROI were obtained in FIJI and plotted using a MATLAB (Mathworks) script color-coded for time (Zajac et al., 2013).

Line scans. A line (width of 1) was drawn across the ER image and subsequently transferred to the Atg13 image at the same exact location, and intensities along each line were determined using the Plot Profile analysis tool in FIJI. A mean background intensity value was determined for each channel by drawing a line outside the cell. The respective mean background value was subtracted from either the ER or Atg13 signals. Each data set was normalized by its own maximum value and expressed as a percentage.

Pearson's Correlation Coefficient Measurements. A maximum projection for the Atg13 movie was generated to draw a line ROI that tracked the biogenesis event. The ROI was transferred to the Atg13 and corresponding membrane movie to generate kymographs (line width of 3) using the Multiple Kymograph plugin in FIJI. Another line ROI (width of 1) was drawn on the Atg13 kymograph over the biogenesis event. Analyzing only the ROI, the Pearson's Correlation Coefficient (without thresholding)

was measured between corresponding kymographs using the Coloc_2 plugin. Values shown in Figure 5C were compared using a one-way ANOVA with a Tukey's post-hoc test. In Supplementary Figure 3, ER kymographs were inverted horizontally and the Pearson's Correlation Coefficient values were compared using a paired t-test.

Supplemental References

Zajac, A.L., Goldman, Y.E., Holzbaur, E.L., and Ostap, E.M. (2013). Local cytoskeletal and organelle interactions impact molecular-motor- driven early endosomal trafficking. Curr Biol *23*, 1173-1180.